Draft compiled: November 3, 2021

Topographic perturbation of turbulent boundary layers by low-angle, early-stage aeolian dunes

Abstract

Decimeter-scale early-stage aeolian bedforms represent topographic features that differ notably from their mature dune counterparts, with nascent forms exhibiting more gently sloping lee sides and a reverse asymmetry in their flow-parallel bed profile compared to mature dunes. Flow associated with the development of these “protodunes”, wherein the crest gradually shifts downstream towards its mature state, was investigated by studying the perturbation of the turbulent boundary layer over a succession of representative bedforms. Rigid, three-dimensional models were studied in a refractive-index-matched experimental flume that enabled near-surface quantification of mean velocities and Reynolds stresses using particle-image velocimetry in wall-normal and wall-parallel measurement planes.

Data indicate strong, topographically-induced, flow perturbations over the protodunes, to a similar relative degree as that found over mature dunes, despite their low-angled slopes. The shape of the crest is found to be an important factor in the development of flow perturbations, and only in the case with the flattest crest was maximal speed-up of flow, and reduction in turbulent stresses, found to occur upstream of the crest. Investigation of the log-linearity of the boundary layer profile over the stoss sides showed that, although the profile is strongly perturbed, a log-linear region exists, but is shifted vertically. A streamwise trend in friction velocity is thus present, showing a behavior similar to the trends in mean velocity. Analysis of the growth of the internal boundary layer on the dune stoss sides, beginning at the toe region, reveals a similar development for all dune shapes, despite clear differences in mean velocity and turbulent stress perturbations in their toe regions. The data presented herein provide the first documentation of flow over morphologies broadly characteristic of subtle,

low-angle, aeolian protodunes, and indicate key areas where further study is required to yield a more complete quantitative understanding of flow–form–transport couplings that govern their morphodynamics.

Keywords

early-stage aeolian dunes, protodunes, turbulence, particle image velocimetry, boundary layers

1. Introduction

Much progress in understanding the controls on aeolian sand dune dynamics has been achieved in recent decades from investigations of aeolian processes operating over mature dune forms (Frank and Kocurek, 1996; Lancaster, 1996; Wiggs et al., 1996; Livingstone et al., 2007). These studies have focused on quantifying the relationships that exist between dune form, airflow perturbations, sand flux, and the subsequent impact of erosion and deposition on dune dynamics. Measurements of flow perturbation over aeolian and subaqueous dunes in both experiments and field environments have revealed the influence of topographic steering by dune morphology on both mean and turbulent flow (Mckenna Neuman et al., 1997; Neuman et al., 2000; Walker and Nickling, 2002; Maddux et al., 2003b; Maddux et al., 2003a; Baddock et al., 2011; Wiggs and Weaver, 2012; Bristow et al., 2018; Bristow et al., 2020; Bristow et al., 2021), and have promoted an understanding of how these forced flow patterns may influence dune migration and growth by driving patterns of sand flux (Bennett and Best, 1995; Best, 2005; Weaver and Wiggs, 2011; Claudin et al., 2013). Studies on the dynamics of mature aeolian dunes have encouraged interest in the development of early-stage dunes, with research examining the controls on the growth of nascent aeolian protodunes into mature dune forms (Nield et al., 2011; Nield, 2011; Elbelrhiti, 2012; Baddock et al., 2018; Delorme et al., 2020; Gadal et al., 2020; Qian et al., 2021).

Early-stage aeolian protodunes are poorly understood bedforms (Kocurek et al., 2010) of the order $\sim$0.04–0.40 m in height (Fig. 1). They have been documented on the margins (Fryberger et al., 1979; Phillips et al., 2019) and interior (Lancaster, 1982) of active dune fields, downwind of linear dunes (Lancaster, 1996), as well as in coastal regions (Cooper, 1958; Kocurek et al., 1992; Jackson et al., 2006; Nield et al., 2011; Baddock et al., 2018). Principally defined by the lack of a slipface (avalanche slope) on their lee-side, protodunes also exhibit wide variability in their longitudinal cross-sectional profile. In contrast to mature dune forms, protodunes can possess a reverse-asymmetry, with a steep windward (stoss) slope and gentle lee slope (Hesp and Arens, 1997; Nield et al., 2011; Baddock et al., 2018). Kocurek et al. (1992) provided a qualitative classification of the dynamics exhibited by early-stage aeolian features as they developed from irregular sand patches, to protodunes, to fully developed dune forms on Padre Island, Texas, USA. They noted that this protodune evolution was characterized by a successive downwind migration of the bedform crest (from an upwind to downwind position), a lowering of the stoss slope angle, a steepening of the lee-slope angle, and a vertical growth in height. This qualitative outline of protodune evolution has been supported by field data (Elbelrhiti, 2012; Baddock et al., 2018; Hage et al., 2018; Phillips et al., 2019).

In order to advance our knowledge of early-stage aeolian bedform dynamics from a qualitative to a quantitative understanding, measurements of the feedbacks between controlling processes on protodune development are required. However, in comparison to investigations on mature dune forms, such process-based studies are particularly challenging in the case of early-stage aeolian bedforms due to their small size. Instrumentation used to measure airflow over dune forms (e.g., cup or sonic anemometers) are of the same order of size as the protodune height. Thus, the disruption to flow caused by the instrumentation effectively obscures the topographically forced flow perturbations that are of interest. Protodune morphologies also evolve relatively quickly, on the order of hours in the earliest stages of development, requiring rapid topographic measurements with sufficient detail to resolve the small changes in form.

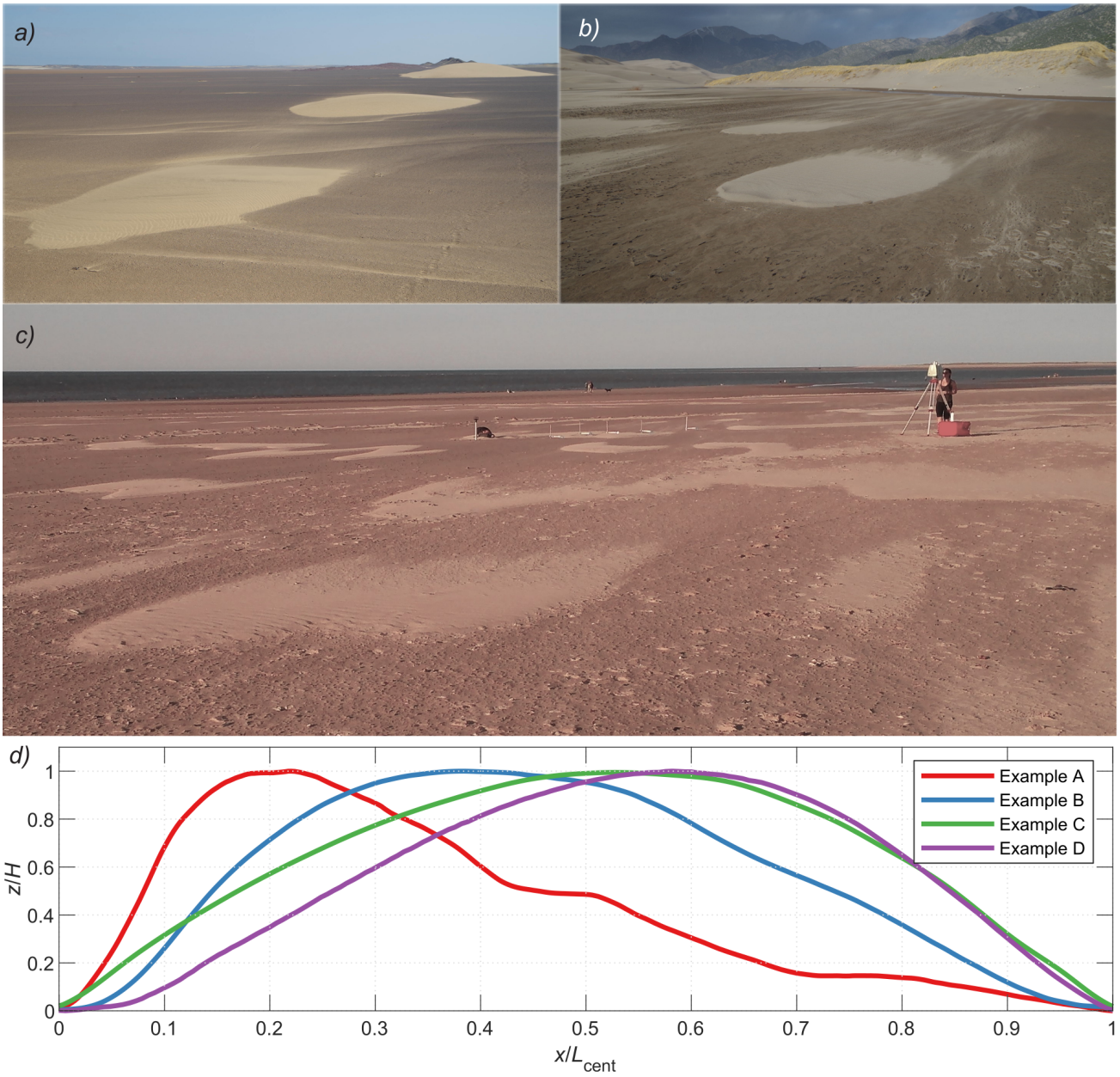

Figure 1: Protodunes in the field from (a) Skeleton Coast National Park, Namibia (foreground bedform), (b) Great Sand Dunes National Park, USA, and (c) Brancaster, UK. Plotted in (d) are the centreline transects from representative protodunes measured by terrestrial laser scanning at Great Sand Dunes (Example A), Brancaster (Example B) and Skeleton Coast (Examples C and D), with x and z scaled by dune length and height respectively. Actual lengths and heights ranged from 2 to 16.5 m and 0.02 to 0.36 m respectively. Flow is left to right in (d).

These difficulties have resulted in process measurements over early-stage dune forms being generally restricted to cases of larger protodunes (c. 0.4 m high). For example, Claudin et al. (2013) measured airflow over a 2-m high, low-angle dune in Morocco using traditional cup anemometers. Qian et al. (2021) reported morphological measurements using a kinematic GPS system for a dome dune in its transition first to a “protobarchan” and then a mature barchan dune, all of which were on the order of one meter in height. These measurements were supplemented by wind tunnel measurements of flow over downscaled models, but the study lacked measurements of sediment transport. In a novel field experiment, Baddock et al. (2018) investigated the morphological development of much smaller (0.06 m high) early-stage bedforms using repeat terrestrial laser scanning (TLS) but, although they obtained particle count-based sand flux measurements, they were unable to measure airflow data to fully examine the form–flow–flux feedback dynamic.

Therefore, while quantitative data on sand flux patterns and morphological dynamics of early-stage aeolian bedforms are beginning to emerge, a significant research gap persists in quantifying the perturbation of airflow caused by the intrusion of such small-scale morphologies into the near-surface atmospheric boundary layer. The aim of the work presented herein is to quantify this flow–form coupling in key protodune development stages by leveraging a refractive-index-matching approach in a laboratory flume environment. This methodology has been demonstrated in recent work to provide high resolution near-surface flow measurements over complex 3D geometries (Bristow et al., 2018; Bristow et al., 2019; Bristow et al., 2020; Blois et al., 2020; Kim et al., 2020; Bristow et al., 2021) by mitigating the obscuring effects of laser reflections during measurements and providing unimpeded optical access for nonintrusive flow quantification with particle image velocimetry (PIV). It is important to note, however, that no sediment transport occurs in this flume environment, and instead the focus is on the flow–form interaction alone utilizing fixed-bed models. Using this approach, we aim to quantify the topographically-induced perturbations in mean and turbulent flow statistics considered relevant for driving sand flux on early-stage aeolian dune surfaces, and examine whether the

resulting flow field is consistent with the occurrence of dynamic feedback processes operating between dune form, flow, and sand flux that might govern early-stage dune development and growth.

2. Methods

2.1 Protodune models

In nature, early-stage protodunes exhibit a wide range of shapes and sizes, and therefore choosing representative protodune morphologies presents a challenge. Rather than reproducing exact replicas of specific protodunes measured in the field, for generality of the conclusions a series of idealized, broadly representative protodunes were developed that captured the key morphological characteristics of most protodunes, while avoiding additional case-specific complexity.

To achieve these aims, protodune models were developed based on a natural protodune measured at Brancaster beach, north Norfolk, UK by Baddock et al. (2018) that was 0.053 m high by 2.02 m long and 2.22 m wide. The "idealization" of this protodune involved first smoothing its morphology with a 0.31 m moving window, which removed superimposed ripples (see discussion of these effects in § 4.2), and then making the morphology spanwise-symmetric about its centerline.

One of the key characteristics of protodune development, as documented by Kocurek et al. (1992), is the gradual adjustment of the crest from an initial upwind position (i.e., with a reverse asymmetry compared to a mature dune) toward a final downwind position (i.e., with regular asymmetry) as it grows. To capture this morphological transition, the crest of the idealized protodune was shifted to four different positions, hereafter referred to as CrestUp, CrestMidA, CrestMidB, and CrestDown (Fig. 2). CrestMidA represented an intermediary stage commonly observed in the field wherein the crest of the protodune becomes relatively flat as it transitions

from the initial upwind position. The aspect ratios of the stoss sides, H/L_{stoss} (where H is the dune height and L_{stoss} is the streamwise length of the stoss side), ranged from $1/8$ to $1/24$, giving relatively low-angled (3–9°) stoss slopes. The dimensions of each model were scaled down such that the height measured approximately 5 mm while retaining the same low aspect ratio of the field protodune, $H/L \approx 1/40$, where L is the full dune streamwise length. The motivation for keeping the heights of the models constant was to maintain the same aspect ratio as well as to allow full immersion of the model within the overlying boundary layer, as dunes in the atmospheric surface layer are generally immersed in the logarithimic region (Supporting Information, § 1).

An additional "Mature" dune morphology case was also included in the experiments for comparison with the protodune datasets. This model had nearly the same morphology as used by Palmer et al. (2012), except that the smoothing filter applied to the protodune models was also utilized on this model. Its centerline transect is shown alongside the protodunes in Fig. 2.

All of the physical dune models were fabricated using a combination of 3D printing and casting. The digital elevation model was first 3D printed using an Objet30 Prime, after which the surface was lightly sanded and polished to remove the "stair-stepping" resulting from the 16 μm deposition layer resolution of the printer. This model was used as the pattern for a cast silicone rubber mold, within which a transparent urethane model was cast. Further details on this approach can be found in Blois et al. (2020).

2.2 Flow facility

Experiments were conducted at the University of Notre Dame in the Large-scale Refractive-Index-Matching (LS-RIM) facility where PIV was used to quantify the flow. The LS-RIM is uniquely designed to handle an aqueous solution of sodium iodide ($\approx 63\%$ by weight) as its working fluid. Refractive-index-matched conditions in the test section are achieved when the refractive indices of the working fluid and any solid model under testing are the same, thus

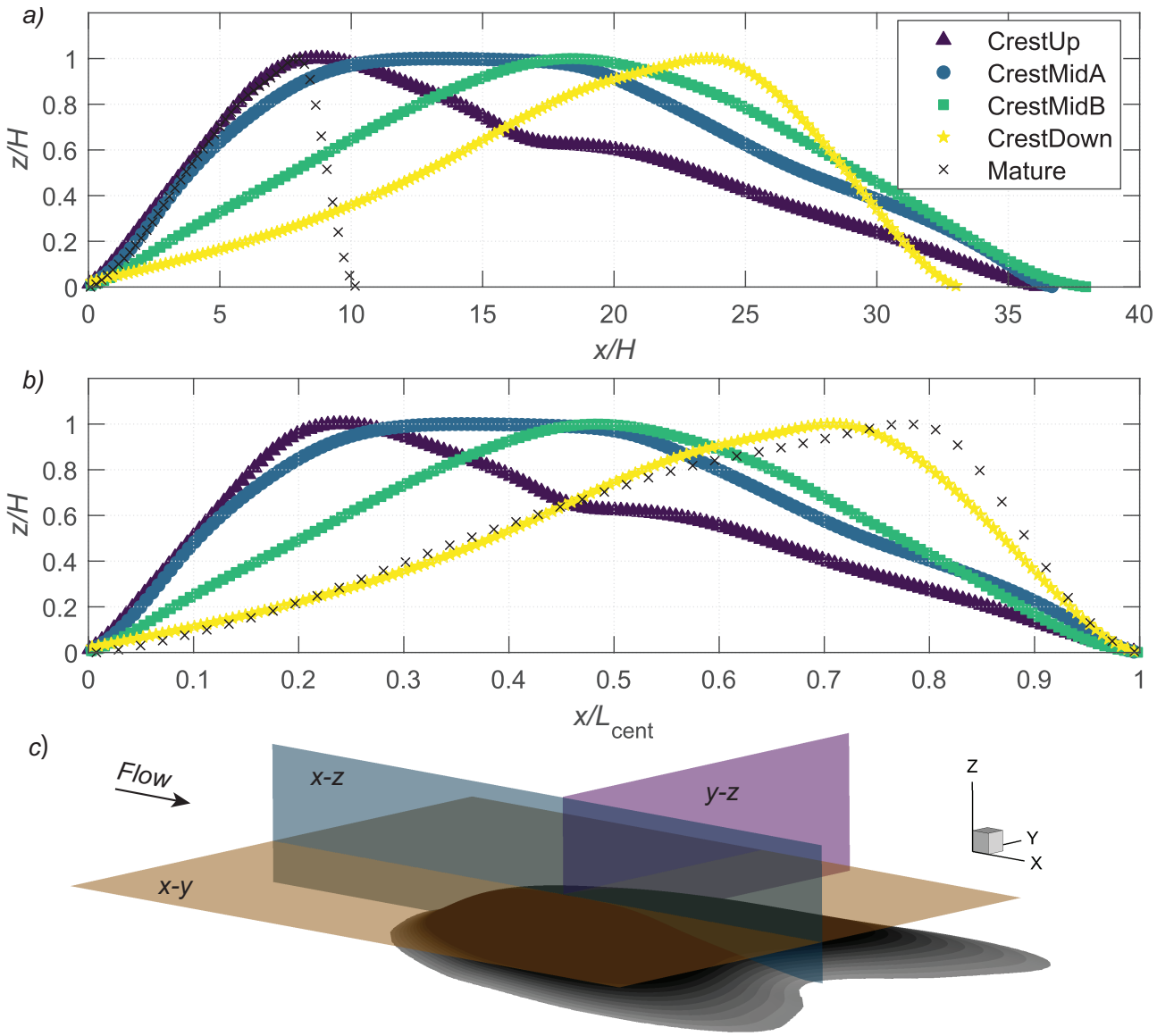

Figure 2: Morphologies of all dunes studied herein along the centerline plane (i.e., $y = 0$), with z scaled by the respective dune height, H, in each case. In (a), the abscissa is scaled by H, while in (b) the abscissa is scaled by L_{cent}, the streamwise length of the topography along the centerline transect shown. Flow is left to right in (a) and (b). Measurement planes over model CrestMidA are depicted in (c), where the z-axis of the model has been stretched to make the topography more visible.

yielding an optical continuum between the two. The advantages of the RIM approach include the mitigation of surface reflections from laser illumination as well as optical distortions as light passes through solid–liquid interfaces. The sodium iodide solution has a high refractive index, closely matching that of the cast urethane models at room temperature, while maintaining a low kinematic viscosity ($\approx 1.1 \times 10^{-6}\,\mathrm{m^2 s^{-1}}$) and thus enabling high Reynolds numbers (Re) to be achieved for the turbulent boundary layers formed on the bottom wall. Further details concerning the facility, and the RIM technique, are described by Blois et al. (2020) and Bristow et al. (2018), Bristow et al. (2019), and Bristow et al. (2020) wherein the same facility was used for measurements over barchan dune models.

The test section of the LS-RIM measures 2.5 m long and 0.45 m $\times$ 0.45 m in cross-section, and at its inlet features a 7 mm tall hemicylinder boundary-layer trip attached to the bottom wall and spanning the entire flume width. At the measurement region, roughly 1.7 m downstream of the inlet, the thickness of the turbulent boundary layer, δ, is 45.8 mm at a free stream velocity, U_e, of 0.97 $\mathrm{ms^{-1}}$, where δ is given by $U(z = \delta) = 0.99U_e$. These flow conditions yield a friction velocity, $u_\star = 0.038\,\mathrm{ms^{-1}}$, and a friction Reynolds number, $Re_\tau = 1600$. The protodune models were immersed within this bottom boundary layer, with the crest well within the logarithmic region at $z/\delta = 0.11$. A more complete discussion of the dynamic similarity between the laboratory facility and the field environment is provided in the Supporting Information § 1.

2.3 Particle image velocimetry

Particle image velocimetry (PIV) measurements were made around the models in the x–z, x–y, and y–z planes , where x, y, and z refer to the streamwise, spanwise, and wall-normal/vertical coordinates, respectively (Fig. 2c). The streamwise–wall-normal plane was aligned with the centerline of the protodune, the streamwise–spanwise plane was located at the crest height, and the y–z plane, for which data were only collected around case CrestMidA, was located at a streamwise position midway along the crest at $x/H = 12.6$ (Fig. 2). Separate

Table 1: Flow variables discussed herein.

	Measurement plane		
	x–*z*	*x*–*y*	*y*–*z*
Mean velocity	U,	U, V^*	U
Reynolds stress	u^2, w^2, uw	u^2, uv	u^2, v^2, w^2, uw, uv, vw
In Supporting Info.	W^*	V^*, v^2	U, V^*, W^*

acquisition systems were used for the flow-parallel (*x*–*z*, *x*–*y*) and cross-stream (*y*–*z*) planes, the details of which are provided in the Supporting Information § 2.

3. Results

In the following analysis, the mean velocities, turbulent stresses, and structure of the logarithmic region of the boundary layer are presented for the different bedform models. Table 1 summarizes the data presented from each of the measurement planes, complemented by additional data provided in the Supporting Information.

3.1 Perturbation of mean velocity

The extent to which protodune morphologies modify the structure of the incoming turbulent boundary layer can be investigated by calculating the disparity between the unperturbed incoming flow and flow measured over the protodune. For data in the *x*–*z* plane, this entailed selecting a vertical profile from the upstream end of the FOV and subtracting this from the profile above the bed obtained at each streamwise position. Similarly, in the *x*–*y* plane, a spanwise profile from the upstream end of the FOV was subtracted, although no topographic shift can be accounted for in this plane, and therefore all data are for the same absolute *z*-position for Δ in the *x*–*y* plane. Thus the disparity of the mean streamwise velocity from the

x–z plane is given by

$$\begin{aligned}\Delta\langle U(x, y=0, z_s)\rangle &= \langle U(x, y=0, z_s)\rangle - \langle U\rangle_{\text{ref}} \\ &= \langle U(x, y=0, z_s)\rangle - \langle U(x=-\infty, y=0, z_s)\rangle,\end{aligned} \tag{1}$$

where z_s indicates a relative height above the surface. For the x–y plane this becomes

$$\begin{aligned}\Delta\langle U(x, y, z=H)\rangle &= \langle U(x, y, z=H)\rangle - \langle U\rangle_{\text{ref}} \\ &= \langle U(x, y, z=H)\rangle - \langle U(x=-\infty, y, z=H)\rangle.\end{aligned} \tag{2}$$

For quantities whose associated reference data were non-zero (e.g., $\langle U\rangle$, $\langle w^2\rangle$), the disparities were normalized with the reference data (i.e., $\Delta\langle U\rangle/\langle U\rangle_{\text{ref}}$), thus yielding a fractional change. For quantities whose time-averaged reference data were near zero (e.g., $\langle V^*\rangle$, $\langle W^*\rangle$, $\langle uv\rangle$), data had to be normalized with another suitable velocity scale, such as U_e or $u_\star$. These are indicated for each figure.

Contour maps of the disparity in mean streamwise velocity, $\Delta\langle U\rangle$, along the centerline (x–z plane at $y = 0$) are shown in Fig. 3. The effect of the topography on $\langle U\rangle$ can be seen in three regions around the protodune: toe, crest, and lee side. At the toe, the flow decelerates relative to the upstream, with the strength of this slow-down consistently decreasing as the crest shifts downstream (i.e., CrestUp to CrestDown). The flow then accelerates up the stoss side, with peak speed-up observed near the crest in all cases. Only in CrestMidA is the maximum acceleration observed prior to the crest, whereas in all other cases the maximum coincides with the crest. Slightly greater magnitude of acceleration is observed over CrestUp and CrestDown, while the speed-up is slightly less in the intermediary cases of CrestMidA and CrestMidB. This appears to be associated with the “flatness” of the crest for CrestUp, which has a very similar stoss side morphology compared with CrestMidA, with the primary difference being that the latter has a very flat crest, likely resulting in a weaker acceleration. In

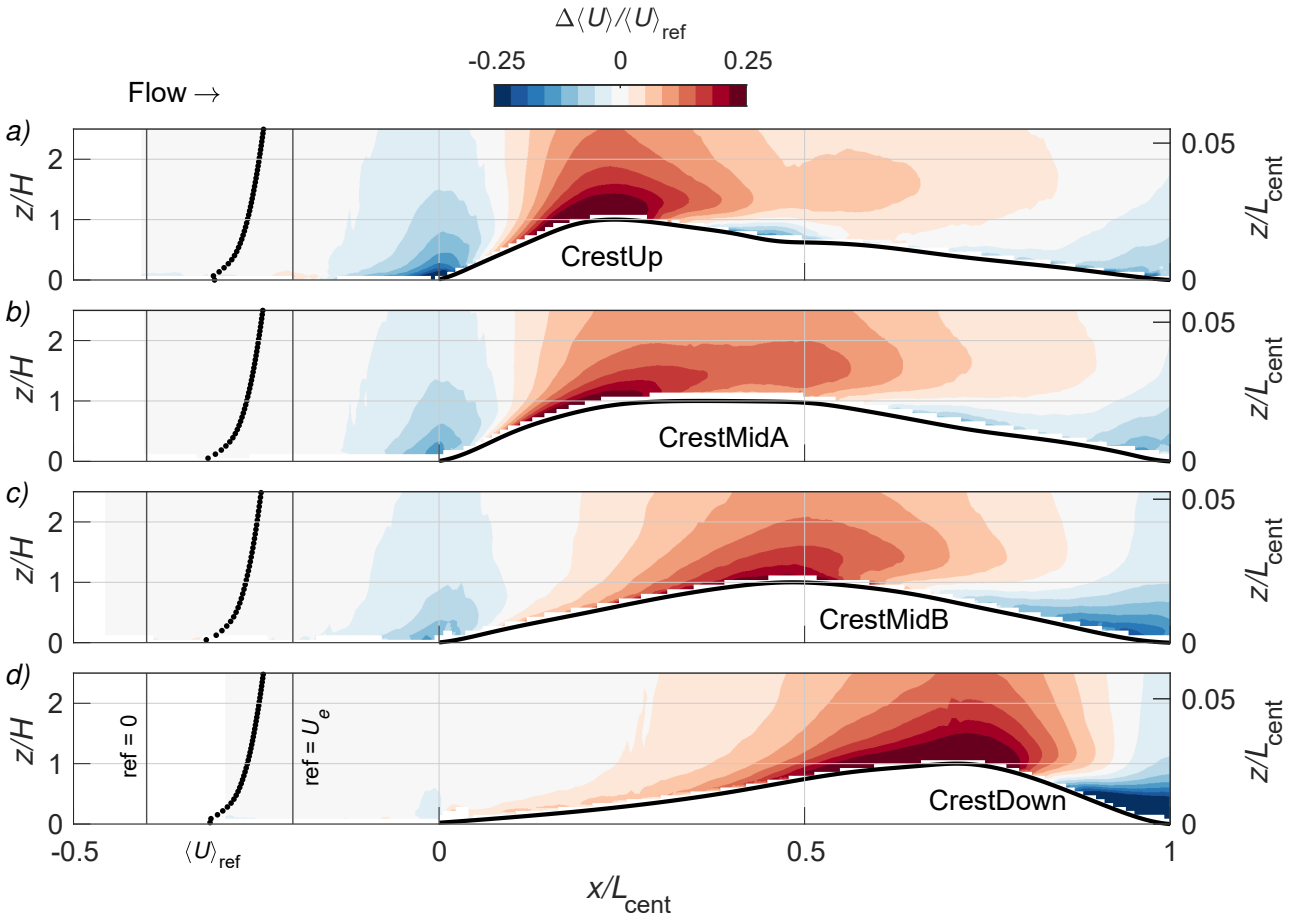

Figure 3: Disparity maps of mean streamwise velocity along the x–z centerline ($y = 0$) plane. Dotted profile overlaid upstream shows reference data used for normalization. Note that the abscissa x is scaled by the streamwise length of the centerline transect topography, L_{cent}, the primary ordinate z is scaled by the respective protodune height, H, and the secondary ordinate shows the scaling of z/L_{cent}. Thus the topography, depicted by the solid black line in each case, does not represent the true aspect ratio of the protodune, which is approximately $1/40$ in all cases. The reference data used to calculate disparity are plotted as a profile on top of the contour maps in the upstream region in order to provide a sense of the magnitudes of the data, which can vary significantly with distance from the surface.

the case of CrestDown, it is less straightforward to draw this same conclusion, as there is no "flat-crested" case to compare to with a similar stoss slope. Regardless, it is noteworthy that despite significant differences in slow-down at the toe, which is much weaker for CrestDown than CrestUp, the acceleration at the crest is still relatively similar across all cases shown.

Beyond the crest, a clear trend in flow deceleration emerges, according to the steepness of the lee side, with CrestDown being the greatest and CrestUp and CrestMidA being the smallest.

Furthermore, the proximity of the crest to the region of greatest flow deceleration changes as well, with the separation between these regions being the smallest for CrestDown. This trend could have implications for deposition and scour in the leeside during development of the dune form: as the region of leeside deceleration gradually shifts closer to the crest, it may further encourage deposition near to the crest and thus reinforce steepening of the leeside slope.

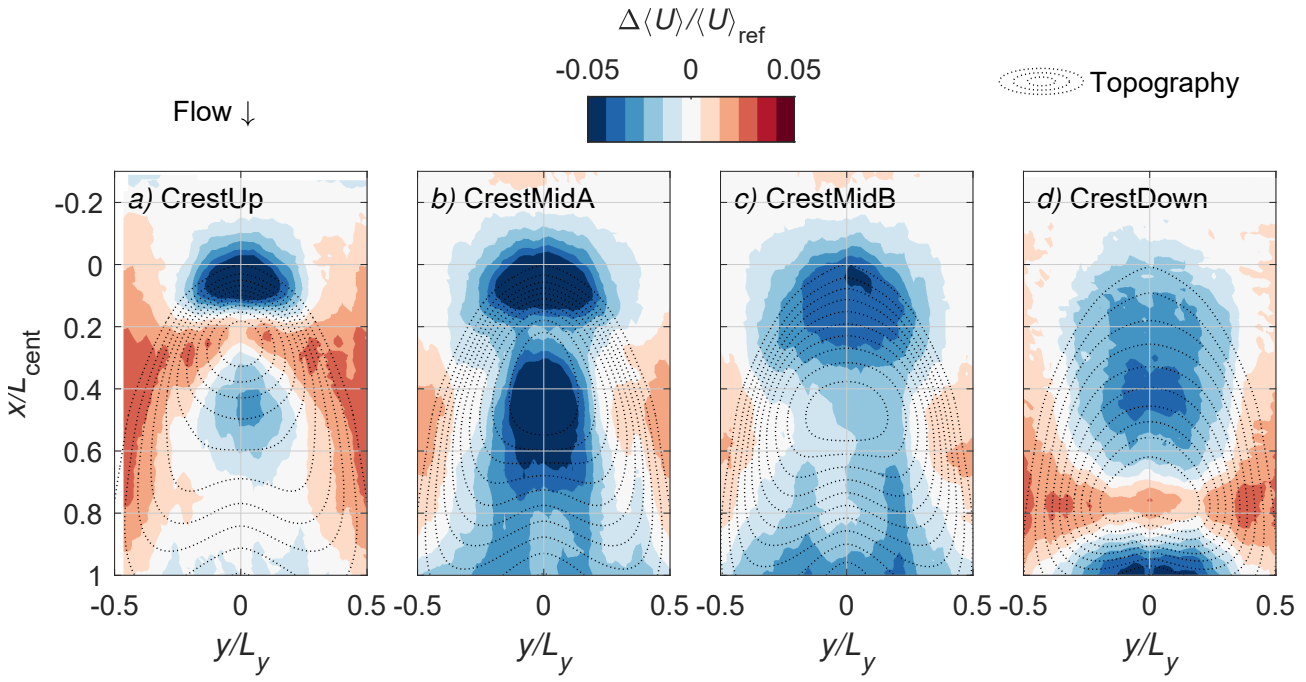

Figure 4: Disparity maps of $\langle U\rangle$ along the x–y plane aligned with the bedform crest ($z/H = 1$). Overlaid dotted outlines show underlying topographies at $0.1H$ increments.

The three-dimensionality of the flow becomes evident in a top-down view of it provided by measurements in the x–y plane (Fig. 4). As mentioned above, the normalization for the x–y plane cannot account for the fact that the distance of the measurement plane from the local topography changes throughout the FOV. Therefore, these disparity maps reflect the difference between the velocities measured at the same absolute height above the wall, but different relative heights above the topography. To aid in this visualization, the contours of the topography are overlaid in each case as dotted lines. One trend in the x–y plane that matches well what was observed in the x–z plane is that CrestUp and CrestDown exhibit the

greatest speed-up of the flow above their crests. Thus in the x–y plane they are the only two cases where $\langle U \rangle$ above the crest (measured extremely close to the local topography, c. 1.0H) exceeds $\langle U \rangle_{\text{ref}}$, despite the reference data having been measured a distance of H above the wall in the incoming flow.

An additional feature that can be seen in all cases from the x–y plane is that the flow accelerates around the sides of the protodunes. Thus the spanwise steering of the flow by the topography locally compresses the streamlines, increasing the momentum of the fluid. All of these changes measured in the x–y plane are, however, relatively small, on the order of 5% maximum, but this is mostly due to the fact that the measurements are largely farther from the surface throughout most of the field of view compared with the x–z plane measurements. The latter plane reveals flow very close to the surface along the entire transect, where perturbations are on the order of 25%. This agrees well with the mean flow perturbations reported by Weaver and Wiggs (2011) and (Baddock et al., 2011) for mature dunes in the field and Charru and Franklin (2012) for a subaqueous experimental barchan. This speed-up is substantially lower, however, than both the measurements of Wiggs et al. (1996), wherein a more sharp-crested morphology was investigated and maximum speed-up of approximately 50% was measured in the field and over 60% in a wind tunnel.

3.2 Perturbation of Reynolds stresses

Perturbation of the turbulent boundary layer is even stronger in terms of higher-order turbulence statistics. Disparity maps of the Reynolds stresses in the x–z plane (Fig. 5–7) show data normalized by the relevant unperturbed flow data from far upstream as an overlain wall-normal profile.

All three measured Reynolds stresses in the x–z plane display an increase in the vicinity of the toe, and decrease over the stoss side, followed by an increase in the lee side. Across the different protodune cases, there is a general trend of decreasing magnitude of disparity

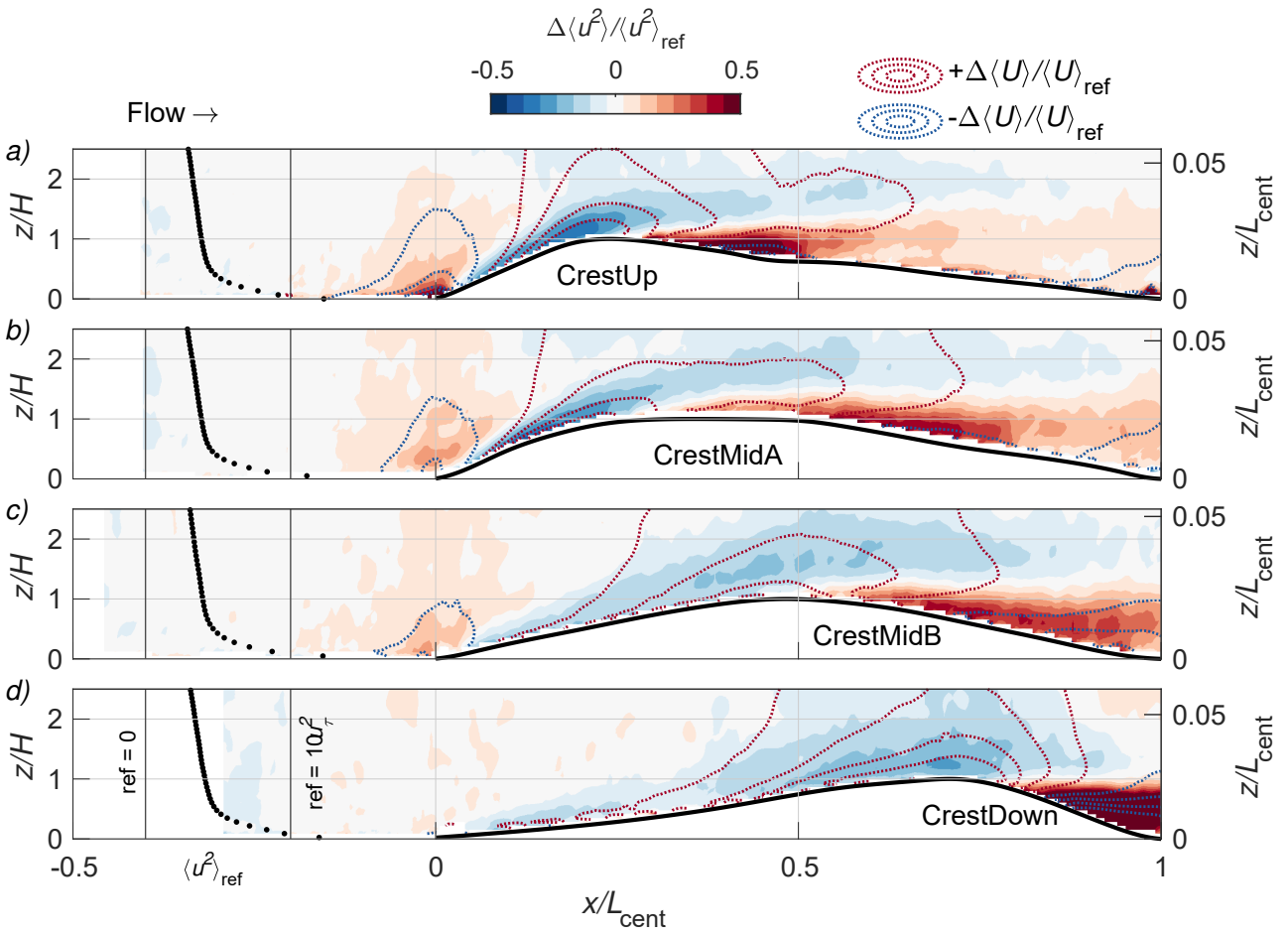

Figure 5: Disparity maps of $\langle u^2 \rangle$ along x–z centerline ($y = 0$) plane. Black dotted profile overlaid upstream shows reference data used for normalization. Blue and red dotted contour lines are overlaid to show coincident disparity of $\langle U \rangle$, spaced at intervals of 0.067.

for a given Reynolds stress in the toe region as the crest of the protodune shifts downstream (i.e., comparing CrestUp through CrestDown). This was the same trend observed for $\langle U \rangle$ in terms of slow-down at the toe. In the lee side, the increase in all three Reynolds stresses is greatest for CrestDown.

The agreement between these trends in Reynolds stresses and results from prior work are more mixed than that of the mean velocity trends. Weaver and Wiggs (2011), who used sonic anemometers to measure flow over mature dunes in the field, reported similar trends for $\langle uw \rangle$ and $\langle w^2 \rangle$, but not for $\langle u^2 \rangle$ for which the perturbation is more subtle and difficult to discern from the field data. Baddock et al. (2011) performed similar measurements as Weaver and Wiggs

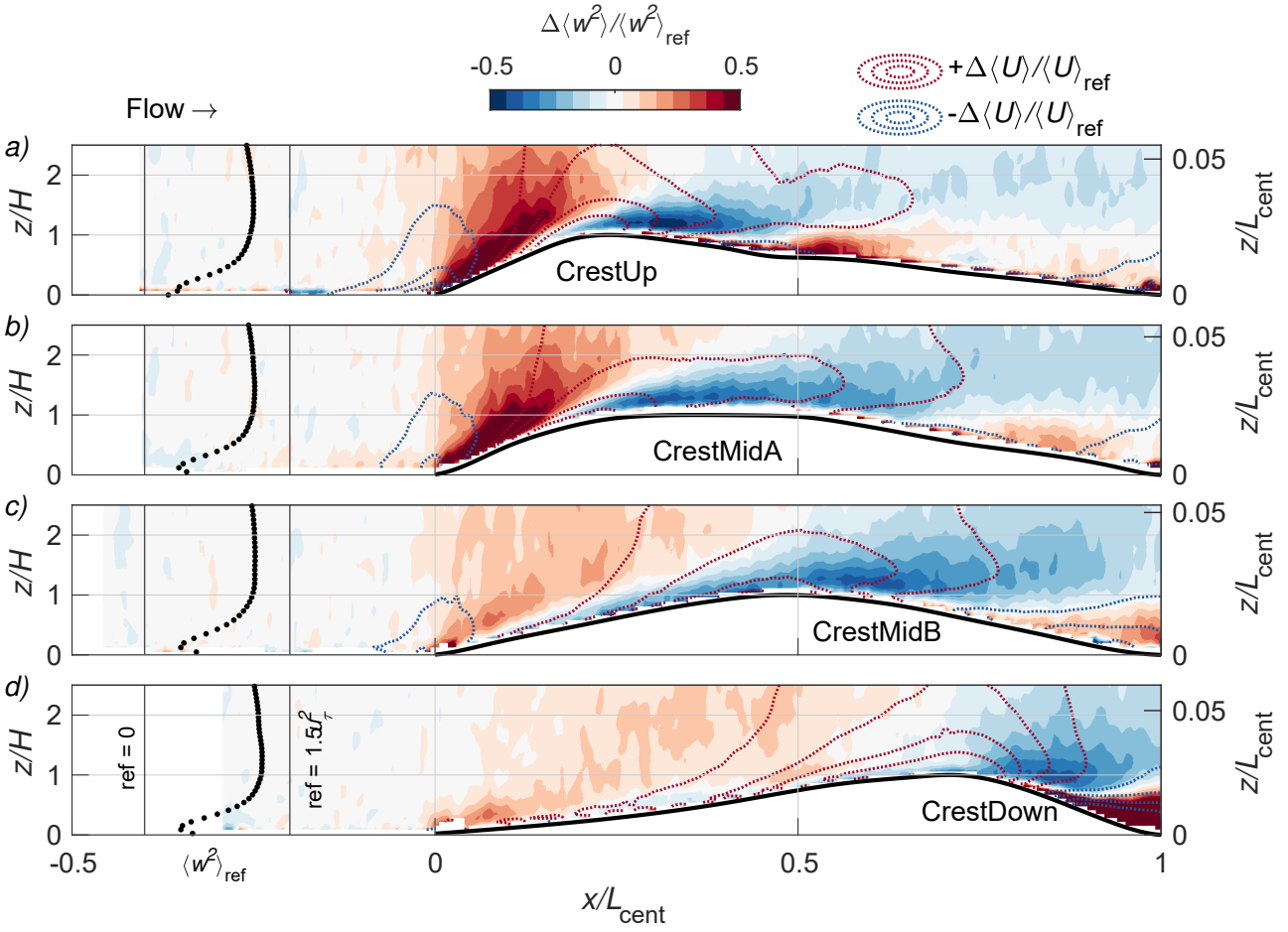

Figure 6: As in Fig. 5, but for $\langle w^2 \rangle$.

(2011), but showed that $\langle u^2 \rangle$ only decreases over the stoss side, with no discernable increase at the toe. This is likely due to the fact that the toe region of their dunes had a very gentle slope, and thus the results resemble those of the CrestDown model herein. Changes to $\langle w^2 \rangle$ and $\langle uw \rangle$ reported by Baddock et al. (2011) are somewhat noisy, but are in general agreement with those presented herein in terms of a mid-stoss transition where the underlying surface curvature changes from concave to convex. Charru and Franklin (2012), in their subaqueous dune experiments, showed good agreement with the trends in $\langle u^2 \rangle$, although their data lacks the toe region, and interestingly for $\langle w^2 \rangle$ showed no variation. Although not specifically dune forms, the gently sloping hill models used by Finnigan et al. (1990) and Webster et al. (1996) in wind tunnels exhibited Reynolds stress trends in close agreement with those reported herein,

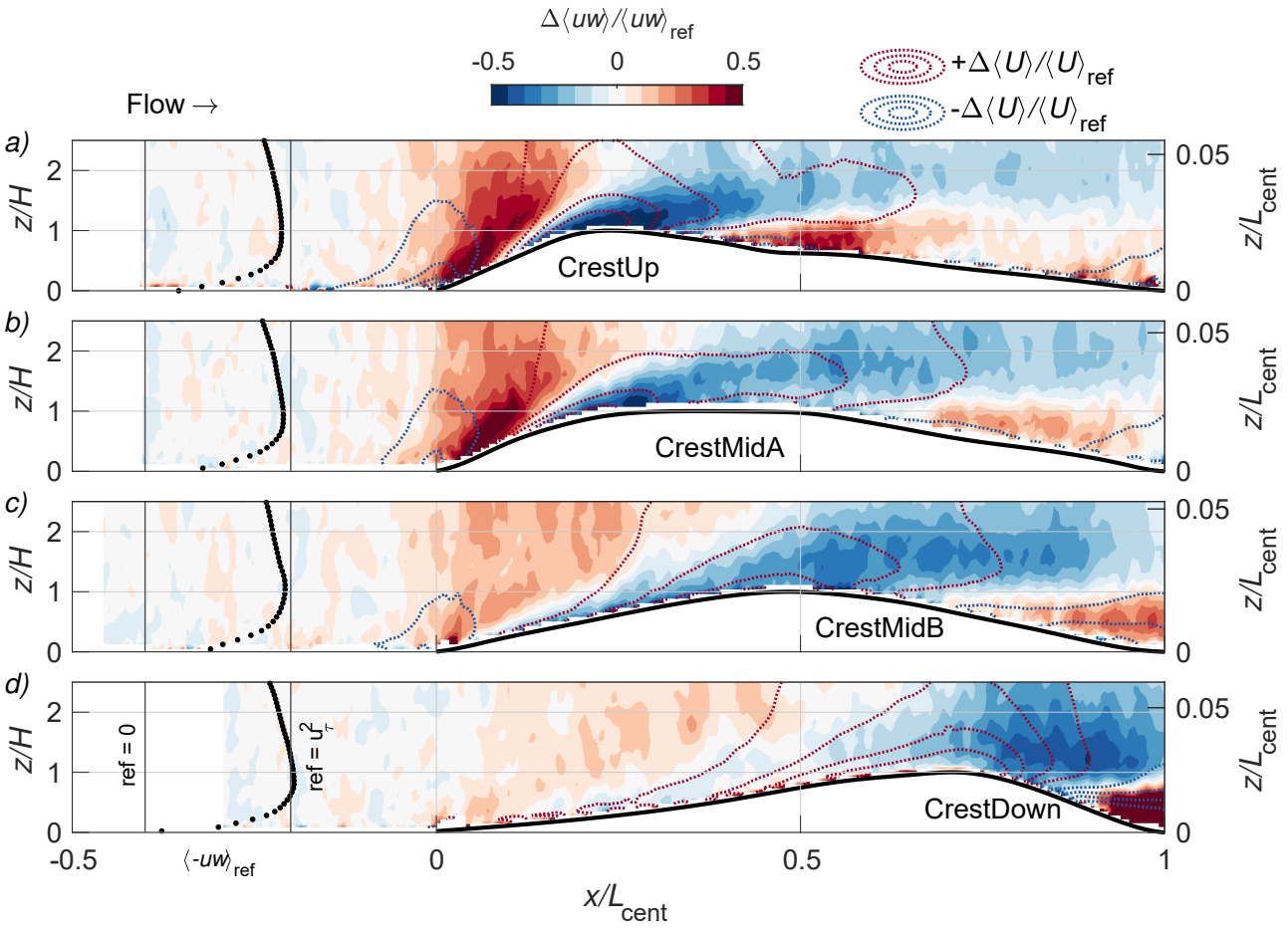

Figure 7: As in Fig. 5, but for $\langle uw \rangle$.

despite having higher aspect ratios (H/L_{stoss}) than the present bedforms.

Comparing the Reynolds stress components for a given protodune case herein, further differences are manifest in terms of the magnitude of the stress disparity and the phase shift relative to $\Delta\langle U \rangle$. Magnitudes of the perturbations to $\langle uw \rangle$ and $\langle w^2 \rangle$ are generally greater than that of $\langle u^2 \rangle$. In terms of the phase, by plotting the dotted contours of $\Delta\langle U \rangle / \langle U \rangle_{ref}$ (and keeping the convention of red for positive disparity and blue for negative disparity) it can be seen that $\langle u^2 \rangle$ is clearly in-phase (though with an inverse relationship) with the speed-up, while the other Reynolds stresses ($\langle uw \rangle$ and $\langle w^2 \rangle$) lag farther downstream. Where $\Delta\langle U \rangle / \langle U \rangle_{ref}$ is negative, $\Delta\langle u^2 \rangle / \langle u^2 \rangle_{ref}$ is positive, and *vice versa*. This relationship is most clear on the stoss side and above the crest region, and somewhat less so for the lee side, except for CrestDown. The

regions of positive $\Delta\langle w^2\rangle/\langle w^2\rangle_{\text{ref}}$ and $\Delta\langle uw\rangle/\langle uw\rangle_{\text{ref}}$ begin immediately after the toe, and thus are more likely associated with streamline curvature, or where $\langle W^*\rangle$ becomes non-zero (see Supporting Information). Such trends can be understood as the effects of streamwise pressure gradients induced by the topography. Although a full exploration of this topic is beyond the scope of the present paper, the reader is directed to the Supporting Information § 8, for further discussion.

Utilizing data from the x–y plane, disparity maps of $\Delta\langle u^2\rangle/\langle u^2\rangle_{\text{ref}}$ and $\Delta\langle uv\rangle/\langle uv\rangle_{\text{ref}}$ show that the in-phase relationship with $\langle U\rangle$ is again particular to $\langle u^2\rangle$ (Fig. 8). To preserve visual clarity, only dotted contours of $\Delta\langle U\rangle/\langle U\rangle_{\text{ref}} = \pm 0.01$ are overlaid in Fig. 8a–d, along with the topographic contour lines.

On the other hand, the spatial trends in $\Delta\langle uv\rangle/u_\star^2$ coincide with $\Delta\langle V^*\rangle/U_e$, as shown by overlaid contours of $\Delta\langle V^*\rangle/U_e = \pm 0.01$. This trend suggests that the streamline curvature imparted by the flow response to the topography is what controls the observed changes in $\langle uv\rangle$ as well as $\langle uw\rangle$. The relationship for $\langle uv\rangle$ is more easily verifiable in the x–y plane through comparison with the mean velocity components since $\langle V^*\rangle$ is both positive and negative, on either side of the protodunes, whereas $\langle W^*\rangle$ is always positive on the stoss side.

The dataset collected from the cross-stream (y–z) plane is particularly valuable in terms of being able to measure all six components of Reynolds stress, and enables further assessment of the effects of bedform three-dimensionality. Due to flow speed-up, indicated by the overlaid red dotted line, a significant reduction in $\langle u^2\rangle$ is noted throughout (Fig. 9a). However, $\langle w^2\rangle$ displays a more complex organization. The near-bed reduction, particularly near the centerline, agrees with measurements from the x–z plane (Fig. 6b). In contrast, near where the topography ends around $y/L_y = 0.4$ there is a region aloft where $\langle w^2\rangle$ increases. This suggests that the increase in $\langle w^2\rangle$ from the x–z plane that occurred at the toe (before the sharp reduction over the rest of the stoss side) was diverted around the sides of the bedform, sustaining increasing vertical turbulent fluctuations in those regions. It is also evident that

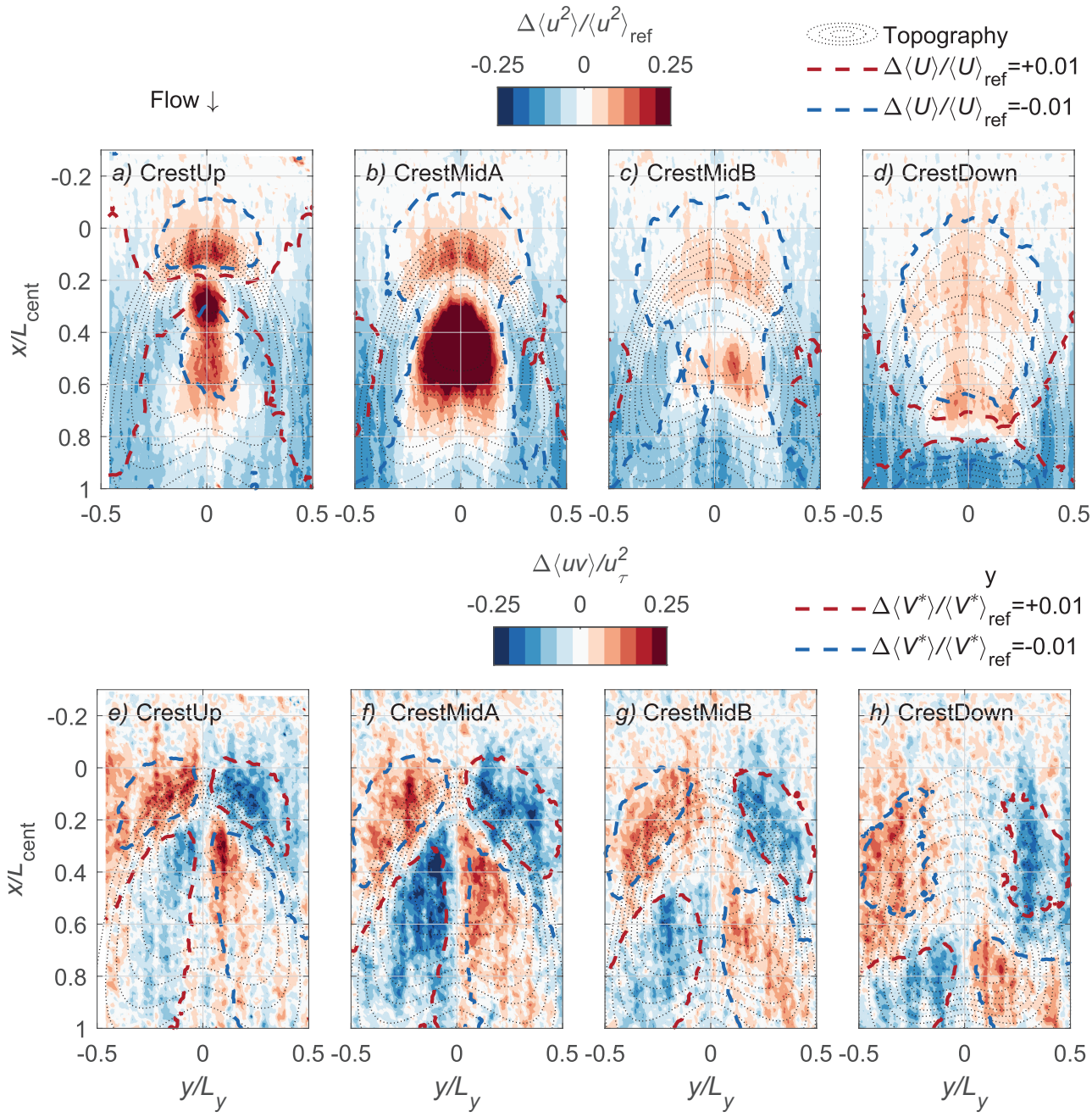

Figure 8: Plan-view disparity maps of (a–d) $\langle u^2 \rangle$ and (e–h) $\langle uv \rangle$ along x–y plane aligned with crest ($z/H = 1$). Gray dotted profile overlaid shows underlying topography, spaced at $0.1H$ intervals. Blue and red dotted contour lines are overlaid to show coincident disparity of $\langle U \rangle$ in (a–d) and $\langle V^* \rangle$ in (e–h).

$\langle v^2 \rangle$ increases the most in this region. Indeed, it is possible that the increased $\langle w^2 \rangle$ and $\langle v^2 \rangle$, along with acceleration of flow around the sides, may be related to the spanwise confinement of such 3D bedforms and the greater mobilization of sediment around the flanks of barchans

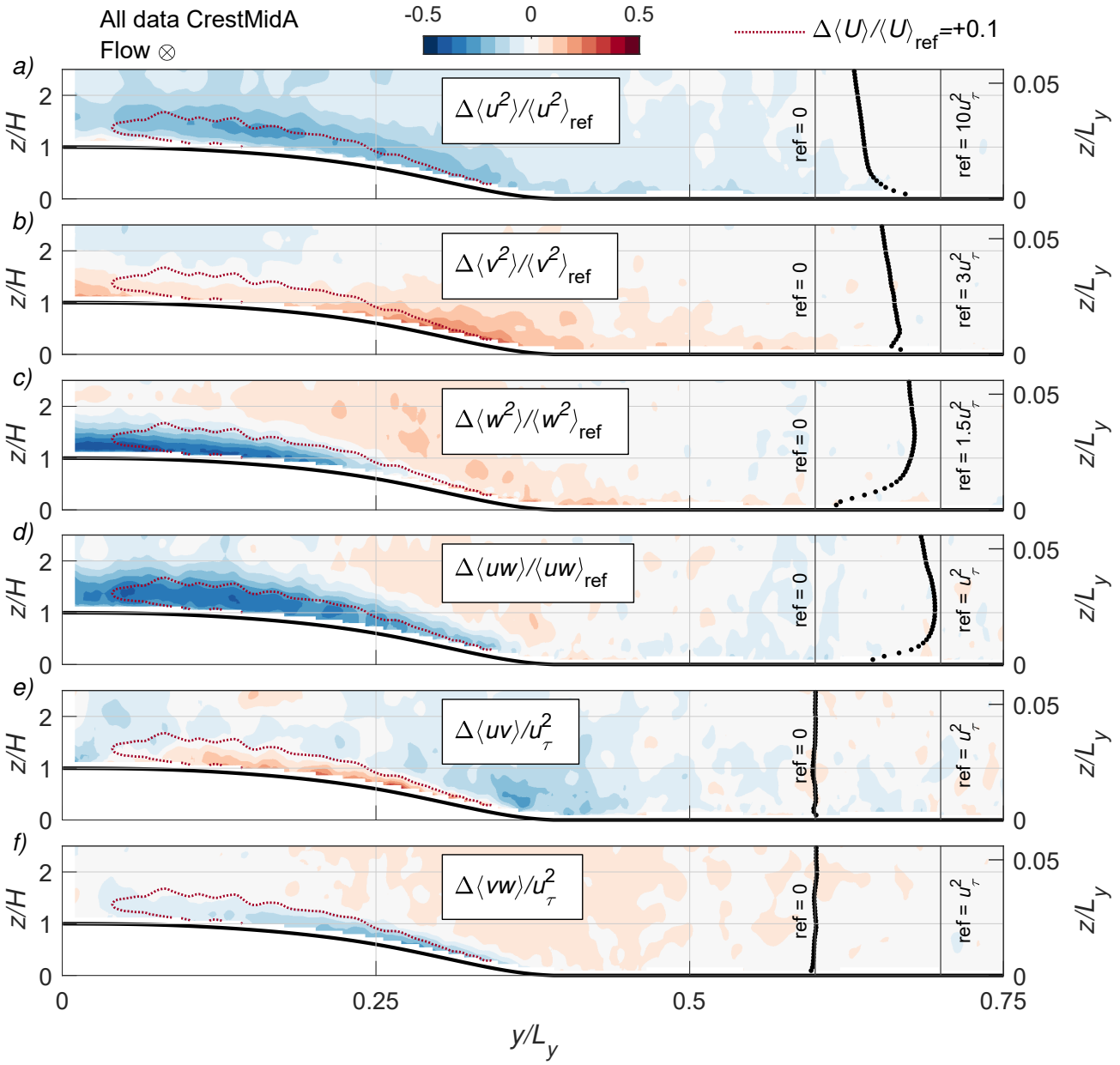

Figure 9: Cross-stream (y–z plane) disparity maps of all six Reynolds stress components for CrestMidA case. Reference data from unperturbed region ($y/L_y \in [0.67, 0.75]$) used to calculate disparity is overlaid on right-hand-side with scale shown. Measurement plane is located at $x = 0.34L_{\text{cent}} = 12.6H$, near the middle of the flat crest. Note that the bulk flow is directed out of the page and L_y is the full width of the entire bedform.

as shown by Alvarez and Franklin (2018).

Changes in $\langle uv \rangle$ and $\langle vw \rangle$ are less intense than the other Reynolds stress components, and are signed opposite from each other. However, each of these quantities are zero in the un-

perturbed region of the flow, and thus a non-zero disparity merely means a non-zero mean value for those stresses. However, both of these stresses also exhibit the most significant changes in this same region near $y/L_y = 0.4$.

3.3 Comparison with a mature dune

To place these results concerning protodunes into context, Fig. 10 presents a subset of the same statistics for flow over the Mature dune case along the x–z plane. The perturbations of the mean velocity and turbulence are very similar to that of the protodunes, at least on the stoss side. Note that the contour levels are unchanged from the protodune disparity maps, and therefore the magnitudes of the changes induced by the bedform are similar. Additionally, the differing phase relationships of $\Delta\langle u^2\rangle$ and $\Delta\langle uw\rangle$ with $\Delta\langle U\rangle$ are similar to the protodune cases. These results are not entirely surprising on the stoss side, as the stoss slope angles of the Mature case are very similar to that of CrestUp (Fig. 2a). Therefore, the similarities and differences noted in § 3.1 and 3.2 concerning the flow over dune forms studied by others (e.g., Weaver and Wiggs, 2011; Baddock et al., 2011) and the protodunes herein also apply to our Mature case.

In the lee side, the effects of flow separation for the Mature case become evident in terms of amplified turbulent stresses. The occurrence of intermittent flow separation here can be compared with the protodune cases (Fig. 11), where instantaneous flow separation is identified at a given grid point if the uncorrected streamwise velocity, U^*, is negative. Separation in the lee side only occurs for CrestDown among the protodunes, and is only then observed in a very thin layer in at most 3% of flow realizations in the ensembles captured. In contrast, the Mature case (Fig. 11b) exhibits nearly permanent flow separation, reaching a maximum of 82% of flow realizations in which flow separation is registered at a given grid point. The highly intermittent nature of flow separation in the CrestDown case may reflect the discontinuous process through which protodunes eventually develop slipfaces, as has been inferred

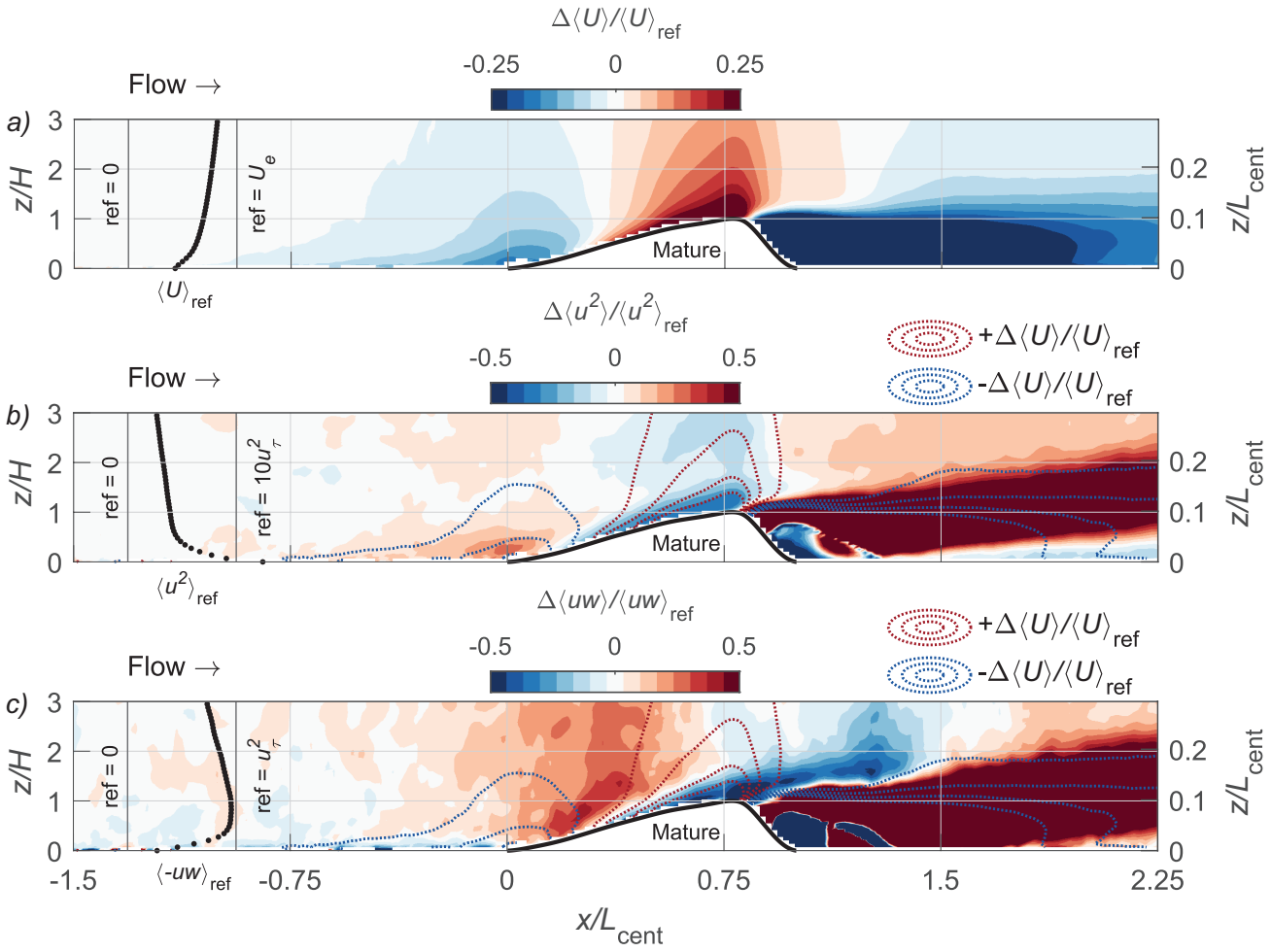

Figure 10: Disparity maps for only the mature dune case of (a) $\langle U \rangle$, (b) $\langle u^2 \rangle$, and (c) $\langle -uw \rangle$. Overlaid contours of $Delta\langle U \rangle / \langle U \rangle_{\text{ref}}$ in (b) and (c) are spaced at intervals of 0.067.

from the stratigraphic record by Phillips et al. (2019). In the transition between CrestDown and Mature morphologies, the slipfaces may develop intermittently until flow separation becomes more permanent.

Due to the nearly-permanent reversing flow in the lee side of the Mature case, the streamline coordinate system transformation renders the results for $\Delta\langle u^2 \rangle$ and $\Delta\langle uw \rangle$ (Fig. 10) in the recirculation region less meaningful, as there should not be a reduction of turbulence in this region. However, it can be seen through much of the rest of the wake that turbulence is greatly increased. Near the wall, beyond flow reattachment ($x \sim 1.25 L_{\text{cent}}$), a thin layer of near-zero disparity in $\Delta\langle u^2 \rangle$ can be observed growing, likely indicative of the new internal boundary layer

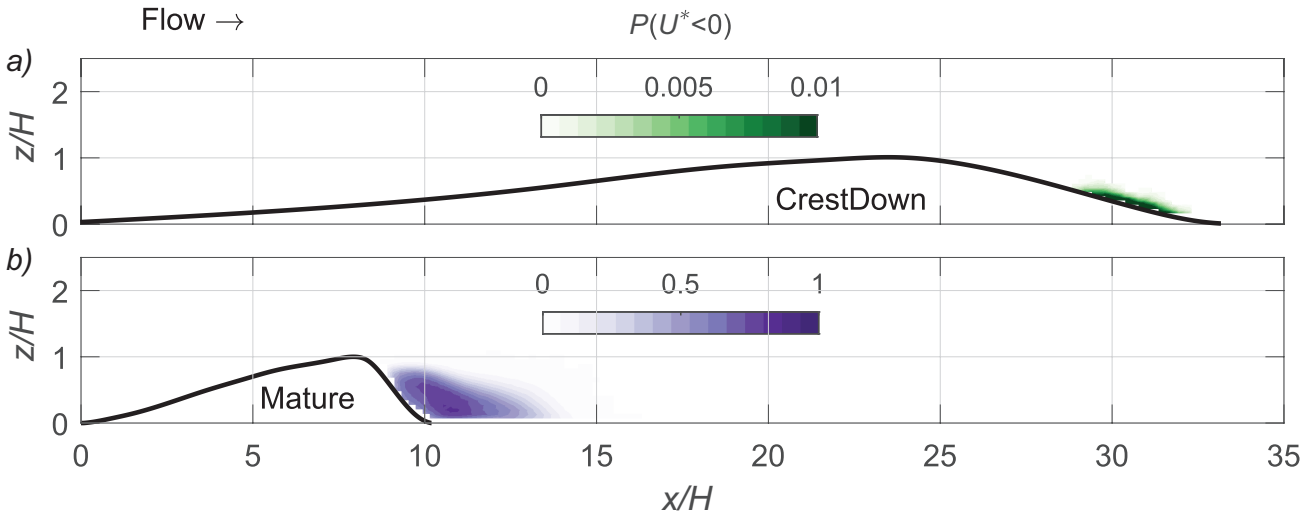

Figure 11: Probability, P, of flow realizations in which negative streamwise velocity (without streamline coordinate system transformation) is measured. All other protodune cases are zero everywhere in the FOV and thus are not shown. Note that the color scales are two orders of magnitude different between (a) and (b).

developing at the wall.

3.4 Constant elevation horizontal profiles

Similarity across all cases for $\langle U \rangle$, $\langle u^2 \rangle$, and $\langle uw \rangle$ on the stoss sides can be assessed more closely with bed-parallel profiles (Fig. 12). A relatively close collapse between CrestUp and Mature is evident over the entire range plotted, although the increase in $\Delta\langle uw \rangle$ for the Mature case is slightly reduced along this profile. As was seen for the disparity maps (Fig. 3, 5, 7) the perturbations to CrestDown and CrestMidB are notably the weakest.

In terms of the trends approaching the crest, a clear difference between CrestMidA and the rest of the cases can be seen for all the statistics shown. In terms of $\Delta\langle U \rangle$, maximum speed-up is reached well before the crest for CrestMidA, and the Reynolds stresses likewise begin to show an upward trend. This is in contrast to the other cases, where $\Delta\langle U \rangle$ only plateaus approaching the crest for CrestUp and CrestMidB, while CrestDown and Mature show continued increases. For the Reynolds stresses, all other cases remain slowly decreasing near the crest, except for CrestMidB, whose profiles plateau. These differences are largely due to

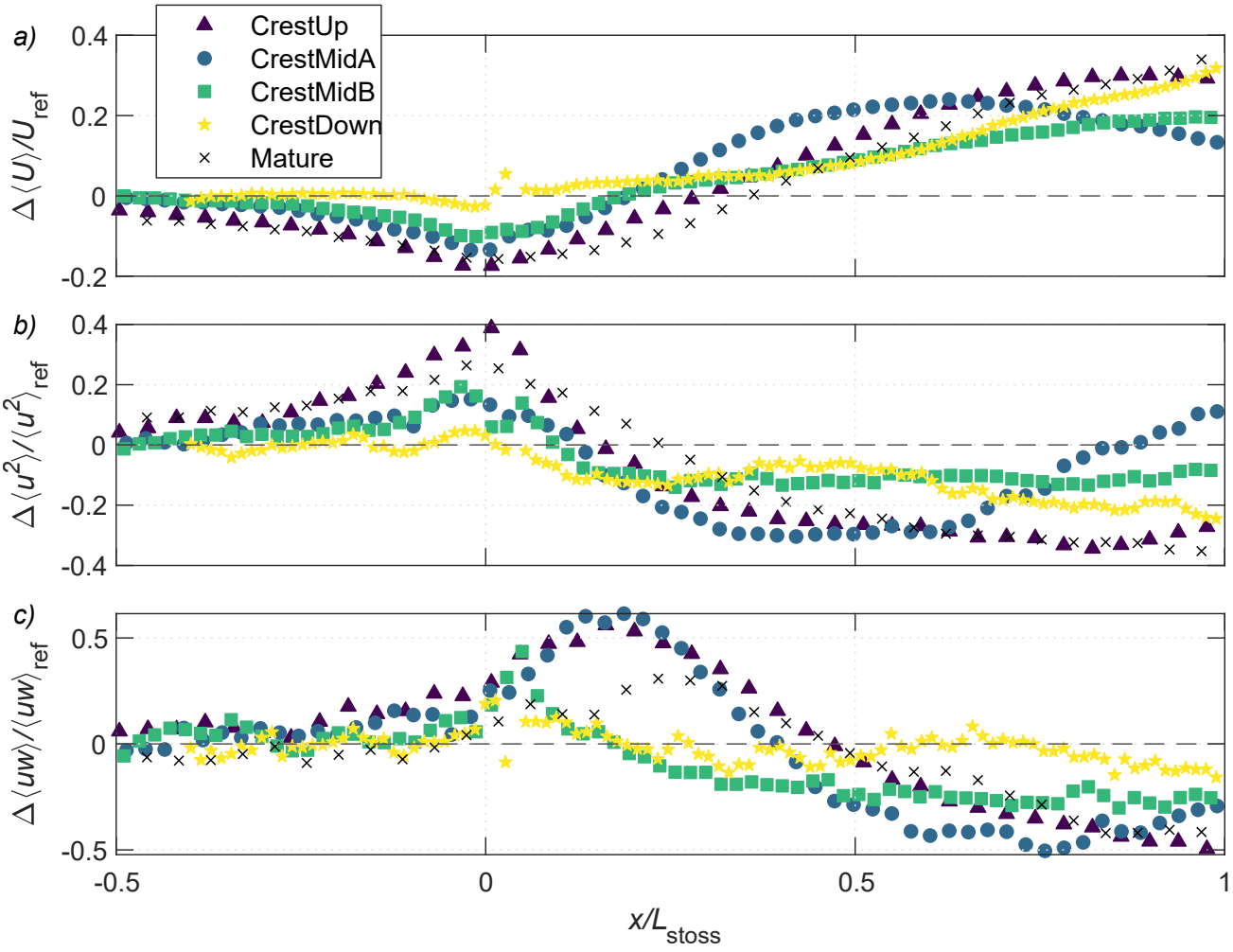

Figure 12: Mean velocity and Reynolds stress profiles from x–z centerline ($y = 0$) plane plotting data from a constant elevation above surface of $z_s/H = 0.2$. The abscissa in each plot is scaled with L_{stoss}, the distance from the toe to crest, where the crest is defined simply as the highest point along the transect.

the fact that CrestMidA has a relatively flat region surrounding the crest point (at $x = 13.1H$, see Fig. 2a). Therefore, before the flow reaches the crestal point, it experiences a very gentle return to a flat surface, resulting in a trend toward the upstream reference values for all of the statistics plotted. This reflects a result similar to that shown by Claudin et al. (2013), where the near-surface maximum flow speed-up was shown to occur ahead (upwind) of the crest and hypothesized to be the condition necessary for bedform growth. The results herein therefore suggest that such mean flow behavior may be dependent on the local curvature of the surface near the crest, such that a weaker curvature in this region induces an upwind shift

of the maximum speed-up and reductions in Reynolds stresses.

3.5 Logarithmic mean velocity profiles

An important metric in flow–form feedback processes is the topographically perturbed mean shear stress at the surface. Under ideal conditions, the log-linearity of the mean velocity profile can be used as a proxy measurement of this stress, but the strong topographic forcing from mature dune forms, and the difficulties of accurately measuring this profile in the field, has complicated the use of this approach (e.g., Mulligan, 1988; Frank and Kocurek, 1996; McLean et al., 2008). Here we leverage the high-resolution access to the flow field with PIV to identify the appropriate log-linear region of the mean velocity profile and then extract the corollary bed shear stress values. A brief background to this topic, as well as details of the approach used herein, are provided in the Supporting Information § 6.

Upstream of each bedform, the mean velocity collapses onto the log law (plotted in green) below $z^+ = 300$, as expected. Deviation in this near-wall region is first shown at the toe ($x/L_{\text{stoss}} = 0$), where deceleration due to the adverse pressure gradient causes the profile to dip below the log law. Beyond the toe, the flow accelerates to be in excess of the log law prediction, for $z^+ < 150$. Interestingly, however, collapse with the log law is not completely lost beyond the toe in the region of flow acceleration, but rather the collapse shifts away from the wall, such that profiles from $x/L_{\text{stoss}} = 0.67$ and $x/L_{\text{stoss}} = 1$ follow the log law within $150 < z^+ < 10^3$.

Therefore, given this relatively good fit (despite the changing region in which log-linearity is observed), the local values of skin friction may be examined. In Fig. 13f, the changes in the log layer-fitted values of $u_\star(x)$ are seen to follow a very similar trend to $\Delta\langle U\rangle/\langle U\rangle_{\text{ref}}$ shown in Fig. 12a. All cases except for CrestMidA show increasing $u_\star(x)$ approaching the crest, in agreement with Walker and Nickling (2003) who measured surface shear stress more directly using surface-mounted differential pressure sensors over transverse dunes in a wind tunnel.

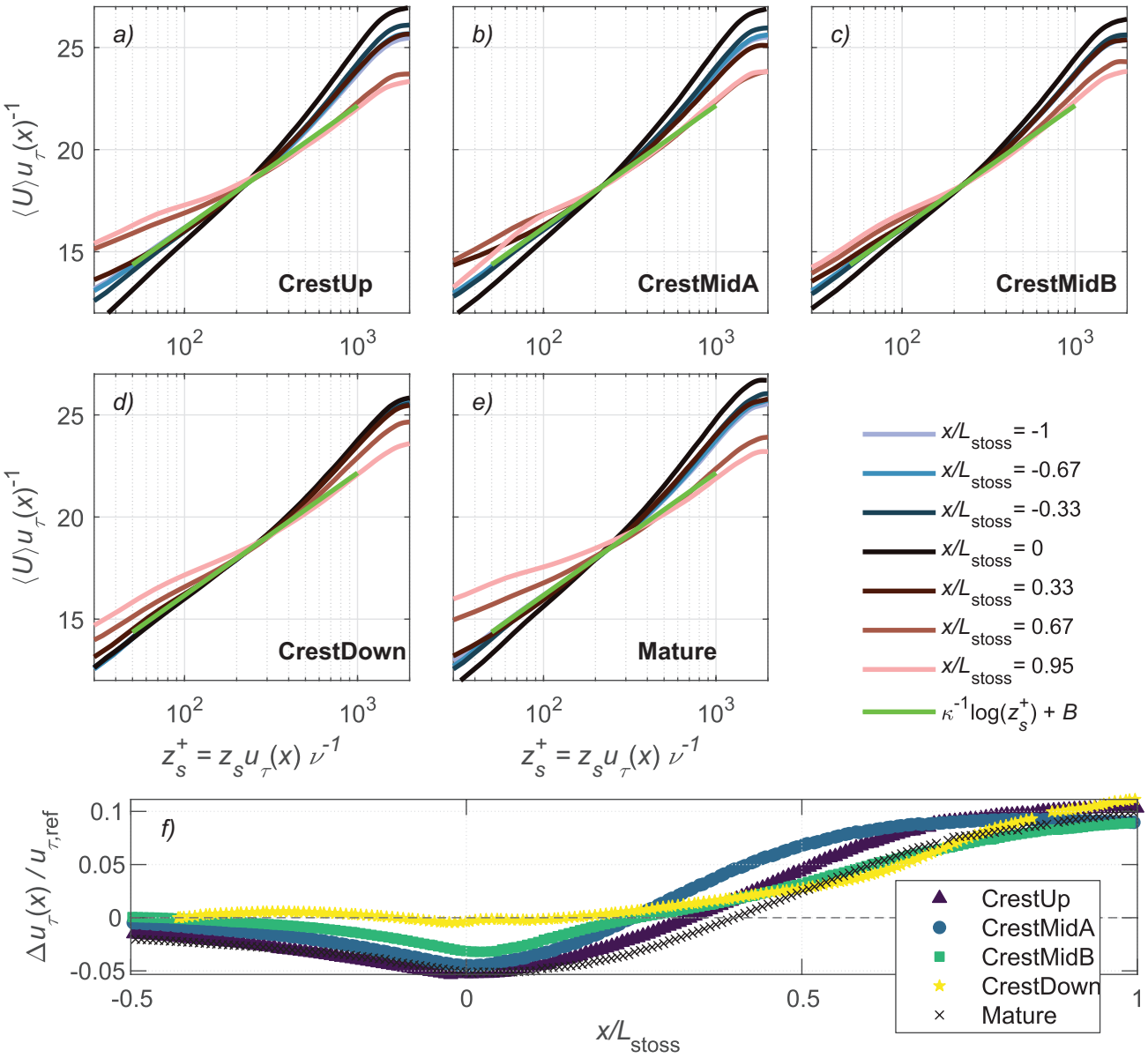

Figure 13: (a–e) Semi-log profiles of $\langle U^+(z_s) \rangle$ from select streamwise positions, and (f) profile of local skin friction values obtained from each streamwise position from the log law fitting.

The morphologies therein featured sharper crests, however, and indeed CrestMidA, which features a more rounded crest, contrasts with these results and possesses a plateau in its shear stress profile. This particular trend for CrestMidA agrees more with Webster et al. (1996), who used oil-film interferometry over a gentle "bump" in a wind tunnel and reported a peak in surface shear stress prior to the crest. Notably, in a field study of flow over the side of a gently sloping dune, Claudin et al. (2013) used measurements of $\langle U \rangle$ very close to the

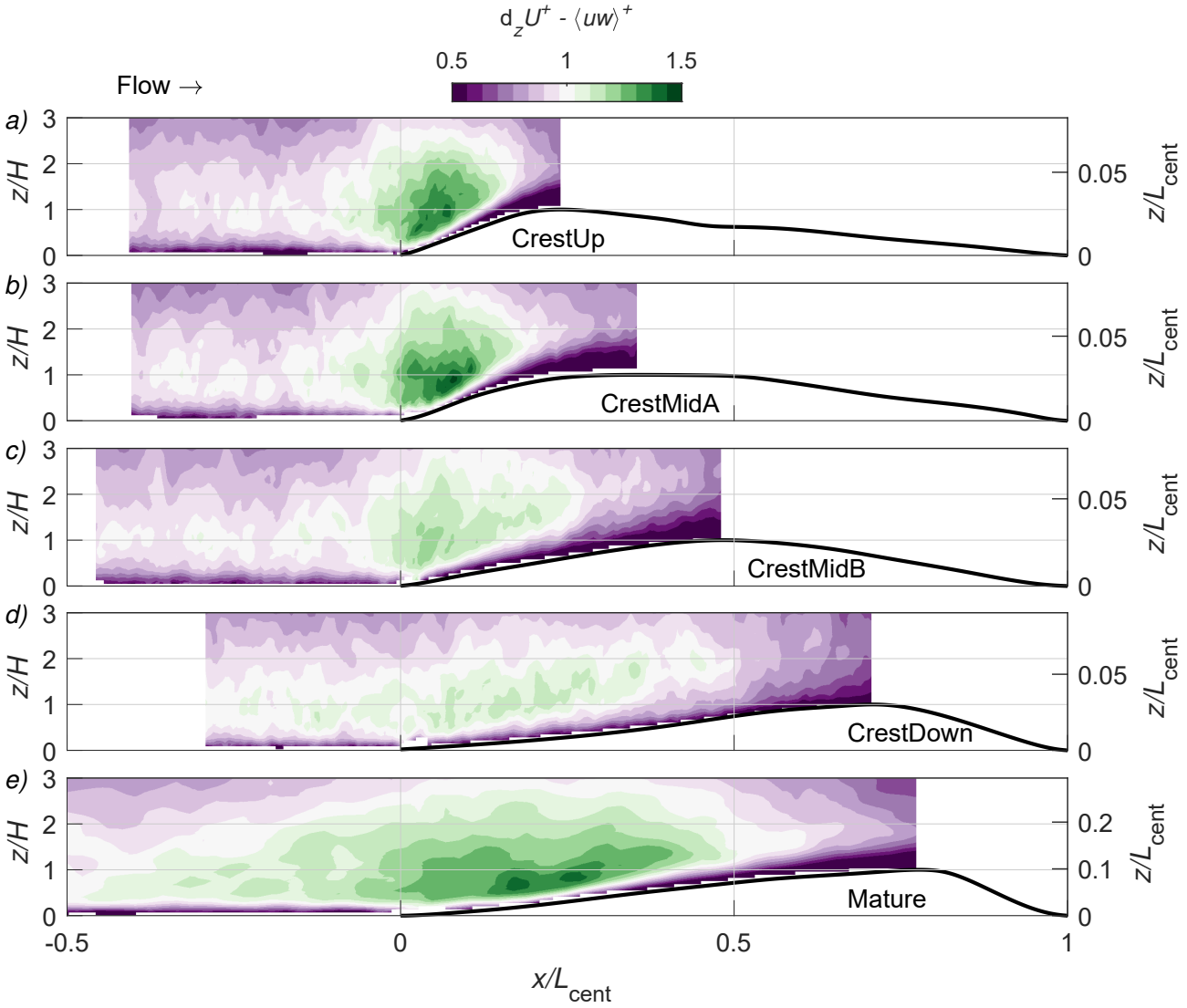

Figure 14: Total shear stress contours normalized in viscous wall units from local skin friction $u_\star(x)$.

surface, within the so-called “inner layer” of Jackson and Hunt (1975), to derive a profile of $u_\star(x)$ similar to that of CrestMidA. Claudin et al. (2013) also used the log law to derive $u_\star$ from a single-point measurement of $\langle U \rangle$, and thus avoided fitting a log law profile. Such a result is perhaps not surprising, given the relatively close agreement shown here between streamwise trends of $\langle U \rangle$ and $u_\star(x)$.

Since the log law profiles herein deviated from the upstream reference profiles, it is worth

examining if measurements of total shear stress, τ/ρ, calculated as

$$\begin{aligned} \frac{\tau}{\rho} &= \nu\frac{\mathrm{d}U}{\mathrm{d}z} - \langle uw\rangle \\ \left(\frac{\tau}{\rho}\right)^{+} &= \frac{\tau}{\rho u_\star(x)^2} = \frac{\mathrm{d}U^{+}}{\mathrm{d}z^{+}} - \langle uw\rangle^{+} \end{aligned} \tag{3}$$

scale appropriately with the local values of $u_\star(x)$. Such contours are plotted in Fig. 14, wherein contours display similar trends to the plot of $\Delta\langle uw\rangle/\langle uw\rangle_{\mathrm{ref}}$ (Fig. 7). The diverging color scale emphasizes non-equilibrium behavior, wherein white filled contours display where the total shear stress normalizes to unity by the local skin friction. In each case, flow upstream of the dune toe features a wall-normal region corresponding roughly with the log layer wherein $\mathrm{d}_z U^{+} - \langle uw\rangle \approx 1$, except for the Mature case where relatively little upstream flow is visible due to horizontal scaling with its shorter centerline. Beginning approximately at the toe, the total stress first increases and then decreases, to varying degrees depending on the morphology, following a pattern similar to $\Delta\langle uw\rangle/\langle uw\rangle_{\mathrm{ref}}$.

These trends imply a breakdown either of $\langle U(z)\rangle$ or $\langle -uw\rangle$ for obtaining a true value of $u_\star(x)$. Given the agreement of the $u_\star(x)$ trends with past studies, it seems likely that the full boundary layer profile is the best proxy herein for τ_0. However, it is unclear if during departure from equilibrium, wherein changes in $u_\star(x)$ coincide with inverse trends in the aloft total shear stress, the mean bed shear stress is the best proxy for sediment flux. Weaver and Wiggs (2011) discussed this disparity in greater detail, noting that increased $\langle -uw\rangle$ at the toe may account for the lack of deposition there, which would otherwise be expected from τ_0. Wiggs and Weaver (2012) explored this further using the quadrant analysis decomposition of uw, and suggested that "sweeps" ($u > 0$, $w < 0$), which increase in frequency at the toe, may sustain transport there while mean velocity drops. Towards the crest, they suggest that an increase in "outward interactions" ($u > 0$, $w > 0$) may help to sustain sediment transport despite the overall reduction in $\langle -uw\rangle$, and thus noted the importance of streamwise turbulence, u, for changes in transport. However, Weaver and Wiggs (2011) reported that strong mean flow

acceleration near the crest is more likely than streamwise turbulence to influence transport behavior.

The upward shift in the log-linear region of the mean velocity profile, combined with the departure from an equilibrium scaling of the total shear stress, suggests that an internal boundary layer may form a very thin layer above the stoss side surface, gradually growing in thickness towards the crest (Frank and Kocurek, 1996). The strongest deviations are associated with CrestUp, CrestMidA, and Mature, particularly near $x/L_{\text{stoss}} = 0$, as they have the steepest stoss slopes of all cases. However, despite the advantages provided by the RIM technique for near-surface flow measurements with PIV, precise identification of an internal boundary layer is challenging. Moreover, no clear differences between protodune cases could be identified in terms of the flow statistics used for delineating internal boundary layers (see Supporting Information § 7 for further details).

4. Discussion

4.1 Morphodynamics

The field measurements of Baddock et al. (2018) provide important context for interpretation of the the flow measurements presented herein. Baddock et al. (2018) measured streamwise profiles of transport and detailed topographic changes as a protodune slightly grew in height and exhibited signs of progression towards a more mature morphology. They showed that the growth of the protodune coincided with a transition from net erosion to deposition upwind of the crest, and that during this process the length of the lee side decreased such that the lee slope steepened. However, Baddock et al. (2018) had no flow data to complement these measurements. The data presented herein help to fill in the gaps as to the potential role of flow perturbations concurrent with these processes, as well as to indicate where additional effects must be considered. In this sense, comparison with the results of Baddock et al. (2018) also serves to constrain the explanatory power of flow measurements in a laboratory environment

devoid of sediment transport.

The CrestMidA case quantified herein is most similar in its morphology to the protodune measured by Baddock et al. (2018). The peaks upstream of the crest for both $u_\star(x)$, derived from the mean velocity profiles (Fig. 13), and $\Delta\langle U\rangle$ (Fig. 3) agree with the expected growth at the crest shown by Baddock et al. (2018). The observation that the other protodune cases herein do not exhibit the same upstream peak suggests that the flow perturbation is most important at this particular stage (CrestMidA). In this sense,it is possible that other effects may be more dominant in other stages such that growth is possible despite the lack of an upstream peak.

The protodune studied by Baddock et al. (2018) also possessed a “bump” on its stoss side that was gradually eroded away during its period of growth on the crest. Based on the flow measurements herein, this is potentially attributable to the sharp increase in Reynolds stresses in this same region (i.e., lower- and mid- stoss, Figs. 5–7). However, such explanations are difficult to accept with certainty as it may be questioned how the flow would generate such a bump in the first place, given that peak Reynolds stresses were also observed for the earlier stage (CrestUp).

The shortening of the lee side observed by Baddock et al. (2018) could be explained by the relatively weak perturbation of mean velocity in the lee side in the early stages of protodune growth where lee slopes are more gentle. Similar to the presumed dynamics in the toe region (Wiggs et al., 1996; Weaver and Wiggs, 2011), deposition at the far edge of the lee side may be inhibited by enhanced turbulent stresses despite a slightly lower mean velocity. Thus, deposition in the lee could be expected to occur primarily closer to the crest, such that the lee side steepens gradually.

The streamwise–spanwise and cross-stream planes (Figs. 4, 8, 9) provide data beyond the scope of Baddock et al. (2018), but their implications require further clarification with field data. The speed-up observed outboard of the crest region in all cases, combined with the

coincident increase in Reynolds stresses at the spanwise edge of topography, suggest that transport should be sustained in this region. This is in agreement with the results of Alvarez and Franklin (2018), who showed greater transport in this region for mobile barchan dunes in a flume environment. Such dynamics may be responsible for the eventual formation of barchan horns. However, this is not entirely clear, as it would suggest that as the crest grows, the side slopes only steepen, which is not necessarily expected to be the case if the overall length-to-width ratio is maintained during protodune development. Thus it is likely that other effects influence this region also, such as the transition from erodible to non-erodible substrate across the lateral edges.

4.2 Remaining questions

Although the well-controlled laboratory environment detailed herein has enabled measurements of the flow over protodunes that are currently impossible to achieve in the field, several critical open questions remain. First, since there is no sediment in the RIM flume, and the models are rigid plastic, conclusions regarding the development of sediment flux over protodunes must be viewed as preliminary. As discussed in § 3.5, the prediction of sediment transport based on flow is not necessarily straightforward, as it is unclear which flow quantity or trends will best predict sediment flux (e.g., mean velocity vs. Reynolds shear stresses). It seems likely that there is no single flow parameter that best predicts flux over the entire bedform. Instead, enhanced streamwise turbulence may compensate for decreased mean velocity near the toe, such that deposition does not occur there (Wiggs et al., 1996; Weaver and Wiggs, 2011; Baddock et al., 2011; Wiggs and Weaver, 2012), similar to the far end of the lee side during steepening prior to a slipface forming.

A related aspect of protodune development that cannot be captured in the RIM environment is the changing height of the bedform relative to an incoming saltation layer thickness. In the earliest protodune stages, where the morphology most closely resembles CrestUp, pro-

todunes in the field are $O(10^{-2} - 10^{-1}\,\mathrm{m})$ high. If saltation activity was to remain unchanged over the extent of the bedform, the CrestUp case would then remain fully immersed within a typical $O(10^{-1}\,\mathrm{m})$ thick saltation layer. As the protodune develops, in addition to the crest shifting downwind (as mimicked in the experiments herein), the dune height also increases such that its crest, in stages CrestMidA and CrestMidB, is higher than the incoming saltation layer. This scaling difference may have an impact on the way sediment flux develops over the streamwise extent of the protodune in its various stages of growth. It is also unclear how the development of an internal boundary layer, as discussed in Supporting Information § 7, may be modified by a saltation layer.

Furthermore, it is also likely that the saturation level for sediment flux changes over the protodunes as incoming sediment encounters a change in the underlying substrate and thus a new transport law (Valance et al., 2013). If the upwind surface is non-erodible, such as a desert pavement, the transition to the erodible surface of the protodune will result in an oversaturation of the sediment flux, causing deposition at some point over the protodune. The associated saturation length (Andreotti et al., 2010) over which this type of transition occurs is not necessarily clear, particularly due to the combined effect of concurrent topographically induced changes to the wind flow. Furthermore, the role of such effects on the lateral edges of a bedform, and their interplay with the flow dynamics there, is unclear. Although such effects would be expected to occur in the context of other dunes morphologies beyond protodunes, it is the relatively short lengths of protodunes, particularly in their earliest stages, that complicates these effects.

Similarly, it is unclear what role linear instability can play in the dynamics of these three-dimensional protodunes at such small scale. The saturation length parameter, related to the lag between flow changes and associated transport modifications, is thought to be an important parameter in determining if a mature dune will grow, as it predicts where deposition will occur relative to the crest (Claudin et al., 2013). However, the saturation length, which is pri-

marily dependent on buoyancy and grain size, is usually $O(10^0\,\mathrm{m})$ in aeolian environments. Although this is not an issue for mature dunes that are $O(10^1 - 10^2\,\mathrm{m})$ in length, for protodunes whose toe–crest separation is $O(10^{-1} - 10^0\,\mathrm{m})$, it is unlikely that the same analytical approach to predicting the growth of the protodune can apply. In the results presented herein, differences have been shown between different protodune shapes concerning the position of maximum mean flow speed-up relative to the crest. However, the scaling issue noted above limits our ability to draw conclusions in the context of linear stability analysis.

It is also worthy of note that the protodunes investigated herein are idealized and do not possess rippled surfaces, which have been proposed to play a role in the growth of dunes (Pelletier, 2009). The superimposition of such secondary bedforms may impact the modification of the boundary layer structure near the surface. However, the general effects of boundary layer perturbation due to non-zero streamwise pressure gradients induced by local topography are unlikely to be altered significantly, despite the presence of ripples as an effective roughness (Finnigan et al., 1990; Webster et al., 1996).

In light of the above considerations, a complete understanding of all the physical mechanisms driving the transitions between protodune development stages remains beyond the scope of the results reported herein. Future advances in understanding appear dependent on further field research that is capable of measuring sediment transport characteristics over additional protodune stages beyond that studied by Baddock et al. (2018). Furthermore, filling in the gap between the final protodune stage considered herein, CrestDown, and the presumed eventual mature dune morphology (the “Mature” case herein), is similarly dependent on field data. Qian et al. (2021) have recently shown such a morphological transition in the field, and complemented these with wind tunnel measurements over solid model replicas, but their work involved no measurements of sediment transport. Therefore, measurements of streamwise profiles of sediment flux over several protodunes throughout the developmental stages would help considerably to close this knowledge gap. Additionally, flow measurements over natural

protodunes, both with and without saltation, could help to elucidate the added effect of particle-loading on the flow, as well as the continuously changing scaling of the protodune height relative to the saltation layer.

5. Conclusions

The use of a refractive-index-matched (RIM) flume has, for the first time, enabled measurement of the turbulent flow field around very small, low-angle protodune models that are representative of early-stage aeolian bedforms. Data suggest that these embryonic dune features are able to significantly steer the flow field, resulting in patterns of mean and turbulent flow that are consistent with measurements of flow-forcing previously observed over mature dune morphologies.

These perturbations include a deceleration of mean streamwise velocity in the toe region of the protodunes, an acceleration on the stoss slope, followed by a slow-down in the lee. It is clear that these flow patterns were considerably altered as the protodune evolved from a crest-up to a crest-down morphology. Although the protodunes exhibit similar levels of streamwise velocity speed-up towards their crests, the curvature of the crest modulates where this effect reaches a peak. Only in the case of the flat-crested CrestMidA protodune was a maximum speed-up observed prior to the crest. Differences in flow in the toe region were more pronounced and showed a clear trend of a reduction in magnitude of deceleration of the flow as the crest shifted downstream and the stoss side sloped more gently.

The perturbations in flow are also manifest in the turbulent statistics, with streamwise Reynolds normal stress ($\langle u^2 \rangle$) showing a clear in-phase relationship with streamwise velocity, and Reynolds shear stresses ($\langle -uw \rangle$) lagging spatially downstream, occurring more in-phase with streamline curvature. The three-dimensionality of the protodunes was found to induce significant cross-stream perturbations in the flow, which were characterized by mean flow acceleration around the flanks of the bedforms, together with a reduction in $\langle u^2 \rangle$ and increase in the other

turbulent normal stresses. The overall patterns of changes to mean velocity and turbulent stresses, both in phase and magnitude, are consistent with flow over the stoss side of a mature dune. However, clear differences are present in the lee side flow due to the effects of flow separation, which only occurs highly intermittently for the final protodune stage with a regular, downstream crest, and not at all for the earlier stages due to the very gentle lee side slope.

The flow perturbations on the stoss side of the protodunes also led to a disruption of the log-linearity of the vertical profile of streamwise velocity and a nonequilibrium scaling of $\langle -uw \rangle$. Although a logarithmic region could be found at each streamwise position along the stoss side, the applicable wall-normal region shifted away from the wall as the crest was approached and the total shear stress decreased. This behaviour suggests that the boundary layer is forced out of equilibrium along the protodune surface due to the pressure gradient and effects of streamline curvature, and associated changes in mean velocity and turbulence. It is not entirely clear if this non-equilibrium behaviour causes the formation of an internal boundary layer over the stoss side of the protodunes, although this seems likely for the most strongly perturbed cases where the crests were in more of an upstream position.

The fixed-bed laboratory data presented herein do not include measurements of sand flux. However, the finding that early-stage bedforms perturb the three-dimensional flow field to such an extent suggests there is potential for their growth to be controlled by feedback processes operating between dune form, flow, sand flux, and subsequent erosion and deposition. This is similar to the process feedbacks considered to operate on mature dune forms. In particular, the present results identify the capacity for a rounded protodune shape to induce an upwind shift in the position of the mean streamwise velocity maximum. Such a finding concurs with field observations of sand flux and surface change on a protodune of similar scaled morphology (Claudin et al., 2013; Baddock et al., 2018).

Nevertheless, whilst the flow perturbations identified in the data presented herein suggest

a potential role for the operation of process feedbacks in the evolution and growth of incipient early-stage bedforms, the scale characteristics of the protodunes are quite different to mature dunes, and this complicates their dynamics. The present study identifies additional complexities that may influence protodune dynamics, including the situation of such early-stage bedforms wholly within the saltation layer, the likely changing rates of sand transport between upstream and on-dune surfaces together with associated spatial lags, and the possible influence of surface ripples that can exist at a similar vertical scale as the underlying early-stage bedform. At the small scales of interest that are important here, such factors are likely to have a proportionately larger impact on protodune dynamics in comparison to larger scale mature dunes. These open questions are not easily resolved in a flume environment where sand transport and micro-morphological features are not scaled in a straightforward manner. However, questions elucidated by such detailed laboratory experimentation indicate a critical path for future field research in order to resolve longstanding questions regarding the initiation and growth of aeolian sand dunes, and providing a generic understanding of the evolution of subaerial and subaqueous bedforms.

References

Alvarez, C. A. and Franklin, E. M. (2018). Role of transverse displacements in the formation of subaqueous barchan dunes. *Phys. Rev. Lett.* 121 (16): 164503.

Andreotti, B., Claudin, P., and Pouliquen, O. (2010). Measurements of the aeolian sand transport saturation length. *Geomorphology* 123 (3): 343–348.

Baddock, M. C., Nield, J. M., and Wiggs, G. F. S. (2018). Early-stage aeolian protodunes: Bedform development and sand transport dynamics. *Earth Surf. Process. Landforms* 43 (1): 339–346.

Baddock, M. C., Wiggs, G. F. S., and Livingstone, I. (2011). A field study of mean and turbulent flow characteristics upwind, over and downwind of barchan dunes. *Earth Surf. Process. Landforms* 36 (11): 1435–1448.

626 Bennett, S. J. and Best, J. L. (1995). Mean flow and turbulence structure over fixed, two-
627 dimensional dunes: implications for sediment transport and bedform stability. *Sedimentol-*
628 *ogy* 42 (3): 491–513.
629 Best, J. L. (2005). The fluid dynamics of river dunes: A review and some future research
630 directions. *J. Geophys. Res. Earth Surf.* 110 (F04S02).
631 Blois, G., Bristow, N. R., Kim, T., Best, J. L., and Christensen, K. T. (2020). Novel Environment
632 Enables PIV Measurements of Turbulent Flow around and within Complex Topographies.
633 *J. Hydraul. Eng.* 146 (5): 4020033.
634 Bristow, N. R., Blois, G., Best, J. L., and Christensen, K. T. (2018). Turbulent flow structure
635 associated with collision between laterally offset, fixed-bed barchan dunes. *J. Geophys.*
636 *Res. Earth Surf.* 123 (9): 2157–2188.
637 Bristow, N. R., Blois, G., Best, J. L., and Christensen, K. T. (2019). Spatial scales of turbulent
638 flow structures associated with interacting barchan dunes. *J. Geophys. Res. Earth Surf.*
639 124 (5): 1175–1200.
640 Bristow, N. R., Blois, G., Best, J. L., and Christensen, K. T. (2020). Secondary flows and vortex
641 structure associated with isolated and interacting barchan dunes. *J. Geophys. Res. Earth.*
642 *Surf.* 125 (2): e2019JF005257.
643 Bristow, N. R., Blois, G., Best, J. L., and Christensen, K. T. (2021). Unsteady dynamics of tur-
644 bulent flow in the wakes of barchan dunes modulated by overlying boundary-layer structure.
645 *Journal of Fluid Mechanics* 920: A51.
646 Charru, F. and Franklin, E. M. (2012). Subaqueous barchan dunes in turbulent shear flow.
647 Part 2. Fluid flow. *J. Fluid Mech.* 694: 131–154.
648 Claudin, P., Wiggs, G. F. S., and Andreotti, B. (2013). Field evidence for the upwind velocity
649 shift at the crest of low dunes. *Boundary-Layer Meteorol.* 148 (1): 195–206.
650 Cooper, W. S. (1958). Coastal sand dunes of Oregon and Washington. Vol. 72. Geological
651 Society of America.

652 Delorme, P., Wiggs, G. F. S., Baddock, M. C., Claudin, P., Nield, J. M., and Valdez, A. (2020).
653 Dune initiation in a bimodal wind regime. *J. Geophys. Res. Earth Surf.*: e2020JF005757.
654 Elbelrhiti, H. (2012). Initiation and early development of barchan dunes: A case study of the
655 Moroccan Atlantic Sahara desert. *Geomorphology* 138 (1): 181–188.
656 Finnigan, J. J., Raupach, M. R., Bradley, E. F., and Aldis, G. K. (1990). A wind tunnel study
657 of turbulent flow of over a two-dimensional ridge. *Boundary-Layer Meteorol.* 50 (1-4): 277–
658 317.
659 Frank, A. J. and Kocurek, G. (1996). Airflow up the stoss slope of sand dunes: limitations of
660 current understanding. *Geomorphology* 17 (1-3): 47–54.
661 Fryberger, S. G., Ahlbrandt, T. S., and Andrews, S. (1979). Origin, sedimentary features, and
662 significance of low-angle eolian “sand sheet” deposits, Great Sand Dunes National Monu-
663 ment and vicinity, Colorado. *J. Sediment. Res.* 49 (3): 733–746.
664 Gadal, C., Narteau, C., Ewing, R. C., Gunn, A., Jerolmack, D., Andreotti, B., and Claudin, P.
665 (2020). Spatial and temporal development of incipient dunes. *Geophys. Res. Lett.* 47 (16):
666 e2020GL088919.
667 Hage, P., Ruessink, B., and Donker, J. (2018). Determining sand strip characteristics using
668 Argus video monitoring. *Aeolian Research* 33: 1–11.
669 Hesp, P. A. and Arens, S. M. (1997). Crescentic dunes at Schiermonnikoog, the Netherlands.
670 *Earth Surf. Process. Landforms* 22 (8): 785–788.
671 Jackson, N. L., Sherman, D. J., Hesp, P. A., Klein, A. H. F., Ballasteros Jr, F., and Nordstrom,
672 K. F. (2006). Small-scale spatial variations in aeolian sediment transport on a fine-sand
673 beach. *J. Coast. Res.*: 379–383.
674 Jackson, P. S. and Hunt, J. C. R. (1975). Turbulent wind flow over a low hill. *Q. J. R. Meteorol.*
675 *Soc.* 101 (430): 929–955.
676 Kim, T., Blois, G., Best, J. L., and Christensen, K. T. (2020). Experimental evidence of ampli-
677 tude modulation in permeable-wall turbulence. *Journal of Fluid Mechanics* 887: A3.

678 Kocurek, G., Townsley, M., Yeh, E., Havholm, K. G., and Sweet, M. L. (1992). Dune and
679 dune-field development on Padre Island, Texas, with implications for interdune deposition
680 and water-table-controlled accumulation. *J. Sediment. Res.* 62 (4): 622–635.
681 Kocurek, G., Ewing, R. C., and Mohrig, D. (2010). How do bedform patterns arise? New views
682 on the role of bedform interactions within a set of boundary conditions. *Earth Surf. Process.*
683 *Landforms* 35 (1): 51–63.
684 Lancaster, N. (1982). Dunes on the Skeleton Coast, Namibia (South West Africa): geomor-
685 phology and grain size relationships. *Earth Surf. Process. Landforms* 7 (6): 575–587.
686 Lancaster, N. (1996). Field studies of sand patch initiation processes on the northern margin
687 of the Namib sand sea. *Earth Surf. Process. Landforms* 21 (10): 947–954.
688 Livingstone, I., Wiggs, G. F. S., and Weaver, C. M. (2007). Geomorphology of desert sand
689 dunes: A review of recent progress. *Earth-Science Rev.* 80 (3-4): 239–257.
690 Maddux, T. B., McLean, S. R., and Nelson, J. M. (2003a). Turbulent flow over three-dimensional
691 dunes: 2. Fluid and bed stresses. *J. Geophys. Res. Surf.* 108 (F1).
692 Maddux, T. B., Nelson, J. M., and McLean, S. R. (2003b). Turbulent flow over three-dimensional
693 dunes: 1. Free surface and flow response. *J. Geophys. Res. Surf.* 108 (F1).
694 Mckenna Neuman, C., Lancaster, N., and Nickling, W. G. (1997). Relations between dune
695 morphology, air flow, and sediment flux on reversing dunes, Silver Peak, Nevada. *Sedi-*
696 *mentology* 44 (6): 1103–1113.
697 McLean, S. R., Nikora, V. I., and Coleman, S. E. (2008). Double-averaged velocity profiles
698 over fixed dune shapes. *Acta Geophys.* 56 (3): 669.
699 Mulligan, K. R. (1988). Velocity profiles measured on the windward slope of a transverse dune.
700 *Earth Surf. Process. Landforms* 13 (7): 573–582.
701 Neuman, C. M., Lancaster, N., and Nickling, W. (2000). The effect of unsteady winds on
702 sediment transport on the stoss slope of a transverse dune, Silver Peak, NV, USA. *Sedi-*
703 *mentology* 47 (1): 211–226.

Nield, J. M. (2011). Surface moisture- induced feedback in aeolian environments. *Geology* 39 (10): 915–918.

Nield, J. M., Wiggs, G. F., and Squirrell, R. S. (2011). Aeolian sand strip mobility and proto-dune development on a drying beach: examining surface moisture and surface roughness patterns measured by terrestrial laser scanning. *Earth Surface Processes and Landforms* 36 (4): 513–522.

Palmer, J. A., Mejia-Alvarez, R., Best, J. L., and Christensen, K. T. (2012). Particle-image velocimetry measurements of flow over interacting barchan dunes. *Exp. Fluids* 52 (3): 809–829.

Pelletier, J. D. (2009). Controls on the height and spacing of eolian ripples and transverse dunes: A numerical modeling investigation. *Geomorphology* 105 (3-4): 322–333.

Phillips, J. D., Ewing, R. C., Bowling, R., Weymer, B. A., Barrineau, P., Nittrouer, J. A., and Everett, M. E. (2019). Low-angle eolian deposits formed by protodune migration, and insights into slipface development at White Sands Dune Field, New Mexico. *Aeolian Res.* 36: 9–26.

Qian, G., Yang, Z., Tian, M., Dong, Z., Liang, A., and Xing, X. (2021). From dome dune to barchan dune: Airflow structure changes measured with particle image velocimetry in a wind tunnel. *Geomorphology*: 107681.

Valance, A., Ho, T. D., Moctar, A. O. E., and Dupont, P. (2013). Scaling laws in aeolian sand transport: Erodible versus non-erodible bed. In: *AIP Conf. Proc.* 1542. (1). American Institute of Physics, 1059–1062.

Walker, I. J. and Nickling, W. G. (2003). Simulation and measurement of surface shear stress over isolated and closely spaced transverse dunes in a wind tunnel. *Earth Surf. Process. Landforms* 28 (10): 1111–1124.

Walker, I. J. and Nickling, W. G. (2002). Dynamics of secondary airflow and sediment transport over and in the lee of transverse dunes. *Prog. Phys. Geogr.* 26 (1): 47–75.

730 Weaver, C. M. and Wiggs, G. F. S. (2011). Field measurements of mean and turbulent airflow
731 over a barchan sand dune. *Geomorphology* 128 (1-2): 32–41.
732 Webster, D. R., DeGraaff, D. B., and Eaton, J. K. (1996). Turbulence characteristics of a
733 boundary layer over a swept bump. *J. Fluid Mech.* 323: 1–22.
734 Wiggs, G. F. S. and Weaver, C. M. (2012). Turbulent flow structures and aeolian sediment
735 transport over a barchan sand dune. *Geophys. Res. Lett.* 39 (5): 1–7.
736 Wiggs, G. F. S., Livingstone, I., and Warren, A. (1996). The role of streamline curvature in
737 sand dune dynamics: evidence from field and wind tunnel measurements. *Geomorphology*
738 17 (1-3): 29–46.